Surface & Coatings Technology 541 (2026) 134065

Contents lists available at ScienceDirect

Surface & Coatings Technology

journal homepage: www.elsevier.com/locate/surfcoat

Linking model tribological tests and milling wear via a specific wear rate descriptor for PVD TiN and TiAlN model coatings☆

Amod Kashyap [a,b,*], Amirmohammad Jamali [c], Finn Rümenapf [d], Nelson Filipe Lopes Dias [d], Vincent Ott [e], Wolfgang Tillmann [d], Michael Stueber [e], Johannes Schneider [a,b], Volker Schulze [c]

[a] Institute for Applied Materials (IAM-ZM), Karlsruhe Institute of Technology, Karlsruhe, Germany
[b] Micro-Tribology Centre (μTC), Karlsruhe Institute of Technology, Karlsruhe, Germany
[c] Institute of Production Science (wbk), Karlsruhe Institute of Technology, Karlsruhe, Germany
[d] Institute of Materials Engineering (LWT), TU Dortmund University, Dortmund, Germany
[e] Institute for Applied Materials (IAM-AWP), Karlsruhe Institute of Technology, Karlsruhe, Germany

ARTICLE INFO

Keywords:
Grey-box modelling
Tool wear
Coated cutting tool, Tribology model test, HiPIMS

ABSTRACT

This work presents a laboratory-scale tribological framework for predicting the flank wear of coated milling tools, developed and validated for monolithic PVD TiN and $Ti_{1-x}Al_xN$ coatings on WC–10 wt% Co inserts in dry milling of normalised C45 steel, using a compact tribological descriptor derived from a ring-on-cylinder model test. For this purpose, a set of DC magnetron-sputtered TiN, TiAlN (Ti:Al 75/25), TiAlN (Ti:Al 50/50), and a HiPIMS TiAlN (Ti:Al 50/50) model coatings was used for both the tribological model and real cutting tests. A commercial TiAlN reference coating was also included in these investigations. The model coatings were simple monolithic coatings with variation of elemental composition, microstructure and morphology, deposited onto cemented carbide model samples and tool inserts. These coatings were characterized by electron probe micro-analysis (EPMA), X-ray diffraction (XRD), and scanning electron microscopy (SEM). All materials were evaluated in both disc-on-ring tests against C45 steel and dry milling of C45 with uncoated and coated WC–Co inserts with regard of the effective wear mechanisms and resulting wear rates. Model tribological tests were designed to reproduce line contact conditions while remaining short in duration (2000 s) and moderate in temperature (up to 100 °C). The rationale behind these model tribological tests was to replicate the wear mechanism occurring in real-world milling, without wearing through the coating completely, so that substrate effects would not influence the prediction of wear in milling experiments. Combined SEM/FIB analyses of worn tribological samples confirmed the dominant wear mechanisms in the model tribotests: diffusion for uncoated, adhesion for TiN and abrasion-dominated wear for Al-rich TiAlN coated samples. These findings very closely matched the wear mechanisms observed on worn milling tools. Consequently, the specific wear rate, defined as wear volume normalised by load and sliding distance, was then used as a coating-specific descriptor (W_s), derived from the model tribological tests. This descriptor was then utilised in a grey-box tool-wear model that combines milling data with thermo-mechanical load scenarios from chip-formation simulations. The resulting framework correctly reproduced the coatings' ranking observed in terms of wear progression during milling and enabled extrapolative prediction of an unseen TiAlN coating using only tribological data obtained from the model tribological test. Compared with a purely data-driven black-box model, the grey-box model achieved a higher R^2 in all coating–parameter combinations and a lower RMSE, with the largest gains at the highest cutting speed and feed, demonstrating that physics- and tribology-informed descriptors can enhance predictive robustness within this material window while reducing experimental effort. Validation is restricted to monolithic TiN/TiAlN coatings against C45 steel; transferability to multilayer, graded or quaternary coating architectures remains to be established.

☆ This article is part of a Special issue entitled: 'ICMCTF 2026 (SCT)' published in Surface & Coatings Technology.

* Corresponding author at: Institute for Applied Materials (IAM-ZM), Karlsruhe Institute of Technology, Karlsruhe, Germany.
E-mail address: amod.kashyap@kit.edu (A. Kashyap).

https://doi.org/10.1016/j.surfcoat.2026.134065
Received 14 August 2026; Received in revised form 15 October 2026; Accepted 21 October 2026
Available online 22 October 2026
0257-8972/© 2026 The Authors. Published by Elsevier B.V. This is an open access article under the CC BY license (http://creativecommons.org/licenses/by/4.0/).
Open access funding enabled and organized by Projekt DEAL.

1. Introduction

Milling processes play a central role in manufacturing industries by enabling precise material removal and surface finishing. The performance and durability of milling tools significantly influence productivity, product quality, and operational costs. Understanding tool wear mechanisms and optimising coatings on milling tools are therefore vital for improving tool life and machining efficiency [1–3]. Conventional milling experiments conducted on full-scale machining machines provide valuable real-world data. However, such experiments are often constrained by high costs, extensive setup time, and machine availability, which limit rapid development and screening of new tool coatings and surface treatments.

The wear behaviour of coated milling tools arises from a coupled influence of cutting parameters, coating chemistry and microstructure, and the local tribological response at the tool-chip and tool-workpiece interfaces. Under milling conditions, the contact is highly transient, with cyclic mechanical loading and steep stress and temperature gradients that make the temporal evolution of tool wear particularly difficult to capture and predict. Although extensive experimental and modelling efforts have clarified many aspects of coating performance and wear mechanisms, reliably predicting wear for different coatings and a wide range of machining conditions remains a significant challenge. Tribological testing in laboratory environments has emerged as a promising alternative to address these challenges. Tribology, the study of friction, wear, and lubrication at interacting surfaces offer model-scale testing methodologies that simulate key wear and friction phenomena of cutting tools under controlled conditions [2,4,5]. By employing tribological tests with milling tool materials or coated tool samples, it is possible to accelerate evaluations of coating performance, analyse wear mechanisms, and optimise surface modifications with greater efficiency and reduced resource expenditure.

Recent studies have demonstrated strong correlations between tribological test results and actual machining performance for various tool coatings such as TiN, TiCN, TiAlN, etc. [6–8]. For example, tribological tests that replicate sliding or rolling contacts typical of cutting edges can reveal coating friction coefficients, adhesive wear characteristics, and coating-substrate adhesion properties, which govern the overall tool behaviour in milling operations. Furthermore, tribometers equipped with modules for scratch adhesion and spiral wear provide detailed insights into coating durability and failure modes, mimicking complex machining interactions while offering precise control over testing parameters [9–11]. Ti-based nitride coatings have been used for decades in the cutting tool industry to enhance lifetime, improve production, and reduce pollution and energy losses. Reactively sputtered TiN was among the first PVD coatings adopted industrially for cutting tools, with early work demonstrating drill-life increases of more than 50-fold over uncoated tools [12]. During this period, the binary TiN (hardness ranging from 15 to 35 GPa [13,14]) coating evolved to the ternary TiAlN (maximum hardness around 35 GPa [15–19]) and quaternary TiAlSiN(hardness around 35–40 GPa [20,21]) coatings for different cutting applications. Apart from these monolithic coatings, a lot of research was also poured into the development of multilayer Ti-based nitride coatings, like Ti/TiN, TiAl/TiAlN [22–24], TiAlSiN/CrAlYN [3,25], etc. The convenctional multilayer coatings were then ugraded to superlattice structures with enhanced mechanical and tribological properties [26–31]. Hovsepian et al. [32] developed TiAlN-based superlattice coatings with a bilayer period of 1.7 nm and reported a significant reduction in the coefficient of friction from 0.90 to 0.65 at temperatures of 850–950 °C. Beyond nitride-based multilayer architectures, alternative interface and top-coat materials have also been explored to suppress built-up edge (BUE) formation and enhance tribological performance. Bobzin et al. [8] showed that a γ-Al2O3 top layer on (Ti,Al)N reduces the coefficient of friction and flank wear relative to the monolithic (Ti,Al)N coating, while Stüber et al. [33] demonstrated that nanocomposite/nanolaminated Ti-Al-N-C coatings suppress built-up-edge formation and improve wear resistance in milling cutting tests. Ibrahim et al. [34] deposited DLC layers through the HiPIMS process over CrN, TiAlSiN, and TiAlN-coated tools, and observed a decrease in interface temperature at the tool chip interface along with the decrease in flank wear. Therefore, extensive research has been devoted to developing advanced coatings to enhance the performance and lifespan of machining tools. While several studies have investigated tool reliability through tribological analyses, to the best of the authors' knowledge, no prior work has focused on establishing laboratory-scale tribological tests capable of evaluating a wide spectrum of coating systems.

Developing reliable laboratory-scale tribology tests tailored specifically for milling tools addresses not only cost and time constraints but also enhances the ability to conduct systematic comparative studies of different coatings and surface treatments. This approach enables high-throughput screening of coating formulations and surface topographies to optimise built-up edge stability and reduce friction-induced wear, ultimately extending tool life and machining productivity. Additionally, tribological testing facilitates microstructural analysis and advanced surface characterisation post-experiment, contributing to a fundamental understanding of coating behaviour.

This work presents a systematic comparison of tribological model test results with milling machine experiments using coated and uncoated tribological samples and milling tools, respectively. The objective is to validate tribological methodologies as efficient proxies for assessing machining performance, which can significantly reduce experimentation costs and durations. The testing parameters were developed following principles similar to those adopted in ASTM standards for tribological and material testing, where short-duration tests under comparatively harsh conditions provide meaningful insight into material performance [35–37]. In the present work, the tribological model tests were performed under dry sliding conditions, thereby creating a severe environment without the need for extreme temperatures or very high sliding velocities. The controlled yet demanding conditions ensured fair comparison among a wide range of coatings. Subsequently, the specific wear rate (W_s) was employed as a tribology-based descriptor to predict wear in milling tools within a grey-box framework [38,39]. Establishing such laboratory-scale tribology protocols will empower tool developers and researchers with rapid, cost-effective tools for coating evaluation, supporting accelerated innovation in cutting tool technology.

2. Materials and methods

2.1. Substrate information

The tribological experiments were carried out using coated and uncoated cemented carbide cylinders with a diameter of 12 mm and 5 mm in thickness. Holes were drilled at the outer edge of the cylinders, 1 mm below the contact surface, to measure the approximate temperature near the contact zone with the help of thermocouples. The substrate was cemented carbide consisting of tungsten carbide (WC) particles bonded with 10 wt% cobalt (Co), with an average particle size of ~0.6 μm, with an average hardness of 1620 HV. The counterface material, a normalised AISI 1045 (C45) was procured from Eisen Schmitt, Germany. A ring-shaped sample was machined out of the C45 discs (Fig. 1(a)). The ring had a diameter of 60 mm and a contact width of 3 mm, and its microstructure consisted of a fine-grained mixture of pearlite and ferrite.

For the milling experiments, uncoated cemented carbide inserts (WC + Co (10%)) inserts (CCHT CCHX09T304E L-11 with the clearance angle of 7° and the rake angle of 10° across all inserts) of hardness 1620 HV were procured from Gühring®, Germany. The corresponding workpiece material was normalised C45 carbon steel, procured from Eisen Schmitt, Germany.

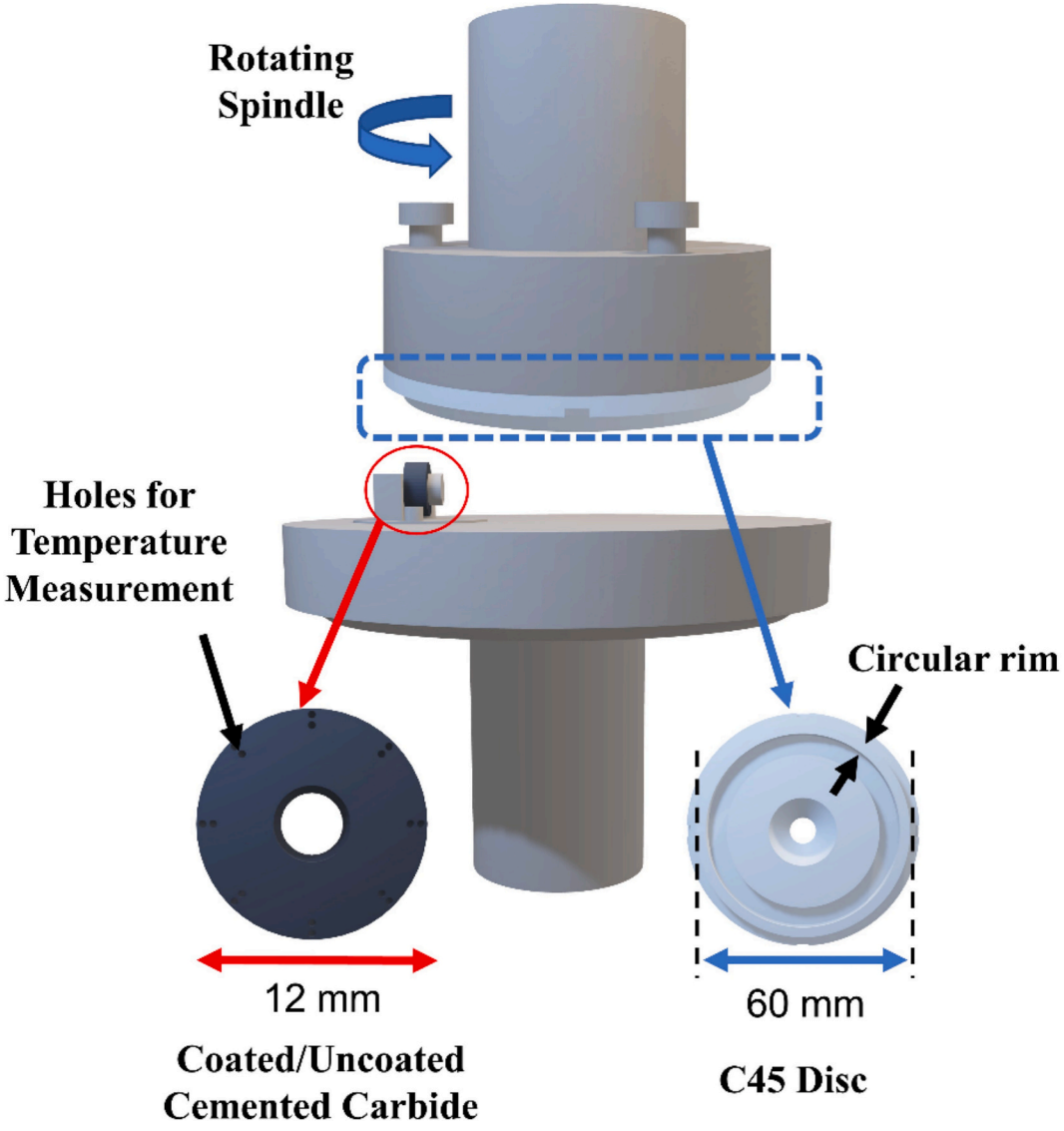


Fig. 1. Schematic representation of the tribological test setup.

2.2. Coating deposition and characterisation

Various in-house model coatings were prepared based on the TiAlN system, with variations in the Ti/Al concentration ratio, coating microstructure, and morphology. The pure TiN, Ti-rich TiAlN(75/25), and Ti and Al-balanced TiAlN(50/50) coatings were deposited by DC reactive magnetron sputtering (DCMS). These single-layer DCMS coatings were produced using reactive sputtering under comparable conditions. A Hauzer HTC 625 system (IHI Hauzer techno Coating B.V., Germany) was used to deposit these coatings. In all cases, the base pressure was maintained below 4×10^{-5} mbar, and the substrates were subjected to plasma etching step of 60 min prior to deposition. The substrates were mounted in a sample holder that, in front of the respective target, rotates them in a two-fold rotational motion. The TiN coating was deposited from a pure Ti target at a temperature of 400 °C, cathode power of 6 kW, an Ar flow rate of 300 sccm, a nitrogen flow rate of 30 sccm, an applied DC substrate bias of −108 V and a deposition time of 300 min. The TiAlN coatings were prepared from alloy targets of compositions of Ti{75}\Al{25} and Ti{50}\Al{50}. The deposition temperature was 600 °C for the TiAlN coatings. The cathode power was 6 kW, and the Ar flow rate was 160 sccm for both the TiAlN coatings. The nitrogen flow rate was 30 sccm for Ti-rich TiAlN(75/25) coating, and 32.4 sccm for TiAlN(50/50) coating. The applied DC bias voltage was 110 V for TiAlN(75/25), and 109 V for TiAlN(50/50), while the deposition durations were 240 min, and 180 min, respectively.

A reactive high-power impulse magnetron sputtering (HiPIMS) process was also used to deposit a TiAlN coating, thereby clearly distinguishing it from the DCMS-deposited coatings with respect to coating growth morphology. This coating was deposited in an Oerlikon Balzers METAPLAS.DOMINO kila flex system (Oerlikon Balzers, Germany) using a Ti{45}\Al{55} target. Similar to the other coatings, the base pressure was kept below 4×10^{-5} mbar, and the substrates were etched for 60 min before deposition. However, the HiPIMS process was carried out at 600 °C with a higher cathode power of 10 kW and pulsed operation characterized by a 100 μs pulse on-time, 900 μs pulse off-time, and 1000 Hz pulse frequency. The Ar and N_2 flow rates were 160 sccm and 45 sccm, respectively. A higher substrate bias voltage of −140 V was applied, with a bias pulse length of 100 μs and a delay time of 30 μs. Due to the lower deposition rate in HiPIMS, the total deposition time was 900 min. Although the target used for HiPIMS deposition was slightly different in composition from what was used for depositing TiAlN (50/50) through DCMS, the elemental composition of Ti and Al found through electron probe microanalysis in the coatings was almost the same for both of the samples. That's why the HiPIMS are referred to as

HiPIMS TiAlN(50/50) later in this article.

Finally, another coating, which served as the industrial benchmark for comparison with all in-house developed coatings, was sourced directly from industry. For this purpose, commercially available TiAlN-based FIRE coated milling tools were procured from Gühring® (Germany). These industrial coatings were not included as a performance benchmark. The in-house coatings were deliberately kept simple and were never tuned or optimised to achieve maximum performance, and the industrial coating acted as a reference material representing the most complex coating case in this study. While the in-house coatings were designed to isolate the effects of composition, constitution, structure and morphology in a controlled, stepwise manner, the industrial coating additionally incorporates professional interface engineering, etching, and top-layer design, making it a suitable test case for evaluating whether the tribological descriptor and grey-box model remain valid as coating complexity increases. These coatings are referred to as industrial coatings (IC) later in the manuscript.

To examine the coatings' morphology, scanning electron microscopy (SEM) (XL3, ThermoFisher, USA) was done on the cross-sectioned samples. For this, the coatings were coated on our model cemented carbide substrates to enable a simultaneous view of both the coating's cross-section morphology and the surface topography. The SEM samples were mounted at a 60-degree angle to the surface normal below the cathode to allow for the simultaneous analysis of the thin film cross-section and the surface topography as well as substrate-layer interface. The accelerating voltage was 15 kV, and the images were obtained using an SE detector.

The X-ray diffraction (XRD) analysis was performed using a Panalytical Empyrean system (Malvern Panalytical GmbH, Germany). The measurement step size in gracing incidence was 0.0231°, with a measurement time of 1 s per step. A PIXEL3D Medipix3 1 × 1 detector was used as a 0D open detector. These measurements covered a 2θ range of 10°–100°. The grazing incidence angle was 2°. Measurements in Bragg-Brentano geometry were performed with a stepsize of 0.0131°, with a measurement time of 150 s per step. The PIXCEL3D Medipix3 1 × 1 was used as the 1D line detector, which allows a measurement range of 3.347° to be analysed simultaneously. The 2θ range covered by these measurements was 10°–100°. The irradiation length of the sample was kept constant at 8 mm by the automatic divergence slit. The raw XRD data were analysed using HighScore software alongside the 'Powder Diffraction Files' (PDF) from the International Centre for Diffraction Data's (ICCD) PDF5+ database, which provided information on phase composition, crystallinity, crystalline structure, lattice plane orientation and texture formation.

The coating variants were selected according to three criteria. (i) Systematic variation of a single coating attribute: TiN, TiAlN (75/25) and TiAlN (50/50) were deposited by the same DCMS process to vary the Al content, and HiPIMS TiAlN (50/50) was added to vary the growth morphology at nearly identical composition, as confirmed by EPMA. (ii) Monolithic single-layer architecture, so that one scalar wear descriptor per coating is physically meaningful. (iii) Availability of the same coating on both tribotest cylinders and milling inserts, so that each coating could be evaluated in both tests. The IC fulfils criterion (iii) but not criteria (i) and (ii); it was therefore included only as an application-relevant reference case and not as a model coating for microstructure-property correlations. Results were included in the evaluation if (a) the wear scar remained within the coating after 2000 s (Table 1), (b) the wear volume could be separated from transferred counterface material, and (c) the test was valid in all repetitions (six for tribotests, three for milling). The following data were excluded, for the reasons stated: the TiN tests at 20 N, because the transfer layer reached the coating-substrate interface and the wear volume could not be determined (criterion (b), Section 3.3); and the specific wear rate of the uncoated specimen at 100 °C from the grey-box model, because the tribofilm formed in the closed ring track prevents the wear of the uncoated specimen in our model tribological tests, which is not the case in the milling tests (Section 3.3).

Table 1
Comparison of maximum wear depth and thickness of the in-house model coatings and IC.

Coating	Thickness (μm)	Maximum wear depth (μm)
TiN	4.9	4.8 ± 0.2
TiAlN (75/25)	4.4	2.8 ± 0.3
TiAlN (50/50)	5.5	1.9 ± 0.2
HiPIMS TiAlN (50/50)	2.1	1.2 ± 0.1
IC	2.0	0.8 ± 0.1

2.3. Tribological model test and analysis

The tribological tests were conducted on a pin-on-disk tribometer (Plint TE-92 HS, Phoenix Tribology, Kingsclere, UK). The disk was machined from C45 normalised carbon steel with a roughness of 0.2 μm, and coated and uncoated cemented carbide cylinders were used in place of the pin (Fig. 1). The disks were machined to create a circular ring of 3 mm width, over which the coated and uncoated cemented carbide cylinders will run (making it a ring-on-cylinder kind of arrangement). The cemented carbide cylinder was oriented so that its load-bearing side was parallel to the axis, resulting in line contact. A normal load was varied from 10 to 20 N over a contact length of 3 mm, resulting in a maximum Hertzian contact pressure of approximately 250–350 MPa. The rotational speed was 15 m/min, and the tests were conducted at temperatures of 25 °C and 100 °C for 2000 s in air. The process for selecting the testing parameters is detailed later in Section 3.3 of the manuscript.

The topographical characteristics of the wear scar were analysed by secondary electron images by dual-beam focused ion beam (FIB), scanning electron microscope (SEM) (Helios NanoLab Dualbeam 650, ThermoFisher, USA), and the wear volume was calculated with the help of a 3D optical profilometer (TopMap Micro View +, Polytec, Germany). Since the wear scars were located on a curved surface, the cylindrical component was first removed to flatten the surface. The flattened surface was then fitted with a best-fit plane. Subsequently, the depth of each pixel within the wear scar was calculated relative to this plane to determine the wear volume. During the initial flattening step, the wear scar region was masked to prevent substrate deformation from influencing the best-fit plane calculation. The elemental mapping was done through energy-dispersive X-ray spectroscopy (EDX) (Oxford Instruments, United Kingdom).

2.4. Milling experiment and analysis

The milling experiments were conducted on the POSmill 1000 CE machine (POS, Germany), and the workpiece was machined from normalised AISI 1045 carbon steel, with dimensions of 100 mm × 100 mm × 150 mm. The axial depth of cut (a_p) and radial depth of cut (a_e) was 2 mm and 0.5 mm, respectively. The experiments were carried out using two cutting speeds, 132 and 112 m/min (v_c), and two feed rates (v_f), 150 and 200 mm/min. In all milling experiments, only one cutting insert (one active tooth, z = 1) was engaged in the cutting process. The feed per tooth (f_z) was 0.34 (v_f = 150 mm/min and v_c = 112 m/min), 0.29 (v_f = 150 mm/min and v_c = 132 m/min), 0.46 (v_f = 200 mm/min and v_c = 112 m/min), and 0.39 mm/tooth (v_f = 200 mm/min and v_c = 132 m/min) for different combinations of v_c and v_f. The experiments were repeated three times. Both milling and tribological experiments were conducted under dry lubrication conditions.

The wear on cutting inserts was measured using a digital light microscope (VHX 6000, Keyence®, Japan). The tool wear defined in the present investigation is the width of the wear scar on the flank face from the cutting edge.

3. Results and discussion

3.1. Coating characterisation

3.1.1. Cross-sectional SEM analysis

Fig. 2 shows cross-sectional SEM images of the in-house model coatings. The TiN coating (Fig. 2(a)) exhibited a pronounced columnar microstructure that is characteristic of PVD films grown in the Thornton Zone-T/Zone-II regime for the given substrate temperature, working-gas pressure and homologous temperature of TiN [14,40,41]. The coating is overall dense, yet individual columns are clearly resolved, enabling a rough estimation of the column width. The columns are tilted relative to the surface normal rather than being strictly perpendicular. Such inclined growth is consistent with oblique-angle deposition, in which the incident flux direction and the sample inclination during coating determine the column tilt. In the present case, the inclination can be attributed to the sample fixturing on the wire holder, which imposed a defined tilt angle during deposition, a configuration that is, in turn, relevant for coating complex cutting-tool geometries with non-normal rake and clearance surfaces. The TiAlN (75/25) (Fig. 2(b)) coating also had a similar dense and columnar microstructure to that of the TiN coating. The Al content didn't seem to have an effect on the columnar structure of the coating. The TiAlN (50/50) (Fig. 2(c)) coating also exhibited a dense, homogeneous columnar morphology, with column widths that appear comparable to those of TiAlN (75/25) and TiN, and thus only weakly affected by the increased Al content. The main difference is observed in the fracture cross-section: where cracks in the previous coating propagated preferentially along well-defined column boundaries, the present coating shows more "smeared" and less sharply delineated intercolumnar interfaces. This might be due to improved intercolumnar cohesion and a reduced tendency for fracture along column boundaries. The fracture surface of TiAlN (50/50) shows less sharply delineated intercolumnar boundaries than that of TiAlN (75/25). We consider differences in intercolumnar porosity, caused by the different growth conditions, to be the most probable cause, since open column boundaries act as preferential crack paths in naturally fractured cross-sections. The porosity was, however, not quantified in the present work, and the observation is therefore not used for further conclusions. The HiPIMS TiAlN (50/50) (Fig. 2(d)) coating exhibited a markedly different surface morphology compared with the DC magnetron sputtered coatings on the same cemented carbide model substrate. The surface topography appears strongly smoothed and "planarized", with the underlying substrate roughness still faintly replicated but largely overlaid by a homogeneous, dense, and essentially featureless coating surface. At higher magnification (see inset of Fig. 2(d)), only a very fine-scale columnar substructure can be discerned, indicating that columnar growth is still present but strongly refined by the intense ion bombardment inherent to the HiPIMS process. Sometimes a large fraction of energetic metal ions in HiPIMS promotes re-sputtering, adatom mobility, and densification, leading to smoother surfaces and suppressed column faceting compared with conventional dc magnetron sputtering operated at moderate substrate bias and predominantly Ar^{+} ion bombardment [42–46].

3.1.2. XRD analysis

Fig. 3 represents the XRD spectra of different in-house model coatings. All coatings are crystalline and show diffraction peaks that can be indexed to the NaCl-type fcc TiN structure ((111), (200), (220), (311) and (222) reflections), confirming that both TiAlN (75/25) and TiAlN (50/50) form metastable cubic $Ti_{1-x}Al_xN$ solid solutions rather than separate TiN and AlN phases [17,18]. Compared with the TiN reference, the TiAlN peaks are systematically shifted to higher 2θ, and the shift is more pronounced for the higher-Al TiAlN (50/50) coating. This behaviour is consistent with substitution of Ti by the smaller Al atoms on the cation sublattice, which reduces the lattice parameter of cubic $Ti_{1-x}Al_xN$ type of coatings [47].

In addition to this solid-solution effect, the coatings exhibit different preferred growth orientations when examined in Bragg-Brentano geometry (not shown). The DC magnetron sputtered TiAlN (50/50) shows a higher relative intensity of the (111) reflection, indicating a (111) oriented columnar microstructure, while the HiPIMS TiAlN (50/50) coating displays a randomly oriented structure. Such changes in the

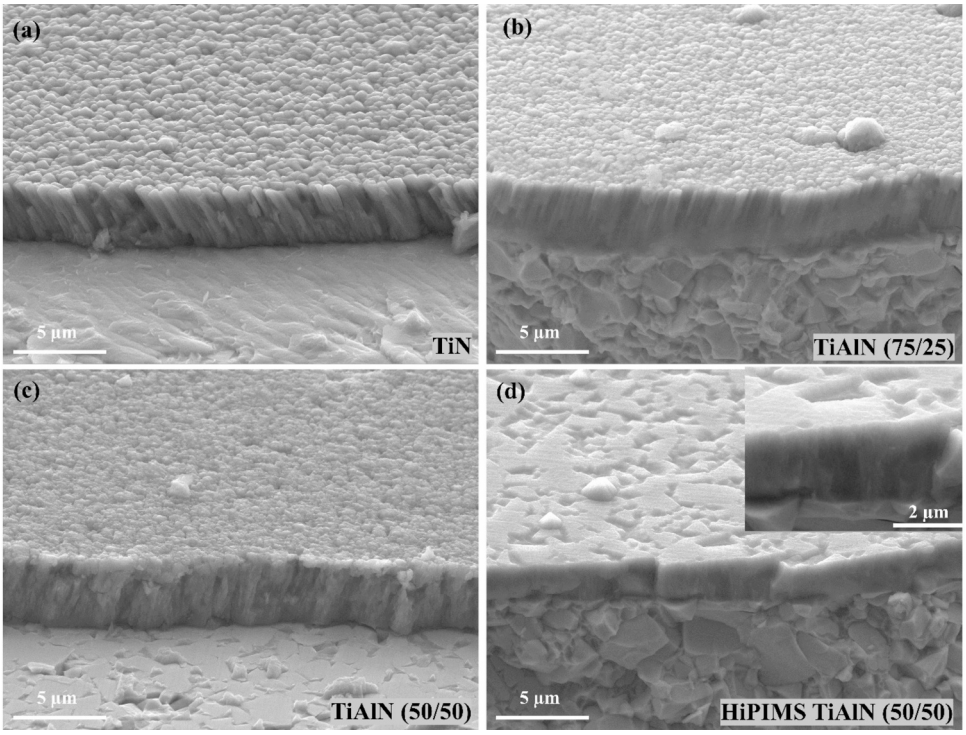


Fig. 2. Cross-sectional and surface topography SEM images of in-house model TiN, TiAlN (75/25), TiAlN (50/50), and HiPIMS TiAlN (50/50) coatings.

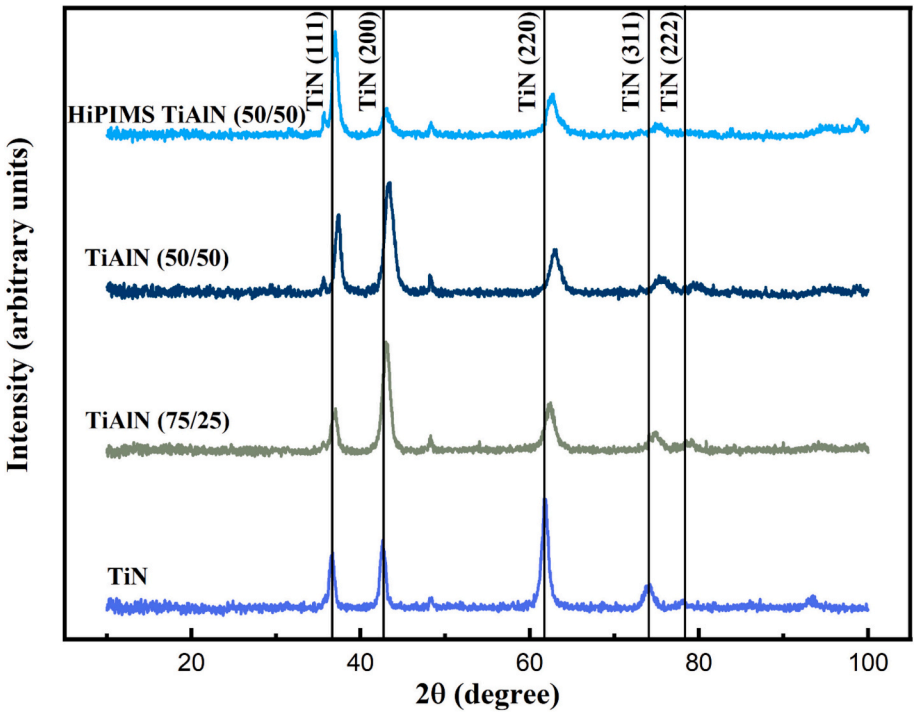


Fig. 3. GI-XRD spectra of in-house model TiN, TiAlN (75/25), TiAlN (50/50), and HiPIMS TiAlN (50/50) coatings on cemented carbide substrates.

preferred growth orientations are well documented for TiAlN: under conditions closer to thermodynamic equilibrium the (111) orientation, has an energetically favoured surface energy in the B1 structure, whereas enhanced ion bombardment and highly energetic fluxes (as in HiPIMS) promote fast growth of multiple nuclei leading to a randomly oriented nanoscale microstructure. Thus, the XRD patterns indicate that all TiAlN coatings are single-phase cubic $Ti_{1-x}Al_xN$, with shifts in the peak position mainly governed by Al substitution and residual stress. The differences in the relative intensities of the diffraction peaks compared to the powder reference pattern (ICDD PDF) reflect the distinct growth textures induced by the conventional DC and HiPIMS deposition processes.

3.2. Milling experiments

Fig. 4 illustrates the progression of flank wear width (VB) for uncoated and coated milling tool inserts under various cutting parameters (cutting velocity (v_c) and feed rate (v_f)) and different surface conditions. Across all cutting conditions, a consistent wear trend is observed, indicating that the relative performance of the coatings remains unchanged. The uncoated insert exhibited the greatest wear progression during the machining tests, whereas the IC-coated insert consistently showed the least flank wear. Among the TiAlN-coated tools, the coating with higher aluminium content demonstrated better wear resistance than the one with lower aluminium content. This improvement can be attributed to the enhanced formation of a protective alumina layer during machining, which helps suppress adhesive wear and slows down tool degradation. In addition, the HiPIMS TiAlN (50/50) coating exhibited lower wear progression than the conventionally deposited TiAlN (50/50) coating under all cutting parameters. Although both coatings had the same nominal chemical composition, their deposition routes led to markedly different microstructures (Fig. 2). The conventional TiAlN (50/50) coating exhibited a classical columnar morphology with thick columns, whereas the HiPIMS TiAlN (50/50) coating developed a very fine-scaled columnar structure, providing improved wear resistance and contributing to its better performance.

3.3. Tribological experiments

The selection of the most suitable test parameters for the tribological experiments began with tests at a normal load of 5 N on the uncoated and IC specimens. Since these two samples were our lower and upper benchmarks, a suitable test duration had to be identified to compare the wear behaviour of all the coatings. As shown in Fig. 5, first, the long-duration tribological tests of 3600 and 7200 s were conducted on the two specimens. It was observed that for the 3600 s test of IC, the coating initially stabilised to a steady-state coefficient of friction of around 0.45, after which, at around 3500 s, the coefficient of friction began to fluctuate again. A similar observation was also seen in the IC when it was tested for 7200 s. The fluctuations increased again around 3500 s for the specimen tested for 7200 s, then stabilised at a steady-state coefficient of friction of 0.42, which was nearly the same as that of the uncoated specimen. Around 3500 s, the coating on the IC specimen began to wear out, and it transitioned to the running-in phase of the uncoated specimen. The x-axis of the uncoated specimen in Fig. 5 was adjusted to show the similar behaviour of IC specimen at around 3500 s. This was confirmed by the optical micrographs of the wear scars. Fig. 6 shows the light microscopy and optical profilometry results of the IC samples tested at 3600 and 7200 s. It can be observed in Fig. 6 (c) that the coating starts peeling off at the end of the 3600 s test. The IC was just 2 μm thick, and the depths up to 2.5 μm can be seen on the wear scar of IC specimen from the colour scale of the z-axis. Therefore, 2000 s was selected as a test duration for the later tests. This test duration ensured that the wear behaviour observed in the specimen was due solely to the coating, with the substrate playing no role.

The investigation was subsequently extended to higher normal loads, with TiN-coated specimens introduced into the testing program at 10, 15, and 20 N. Fig. 7 shows the evolution of the coefficient of friction for the uncoated, TiN-coated, and IC-coated specimens at room temperature (25 °C) under loads of 10 N, 15 N, and 20 N. The friction responses for the specimens were averaged over six repetitions; the average coefficient of friction is shown in a darker shade, while the standard deviation across tests is shown in a lighter shade. A common frictional response was observed across all test conditions, with an initial rise in the

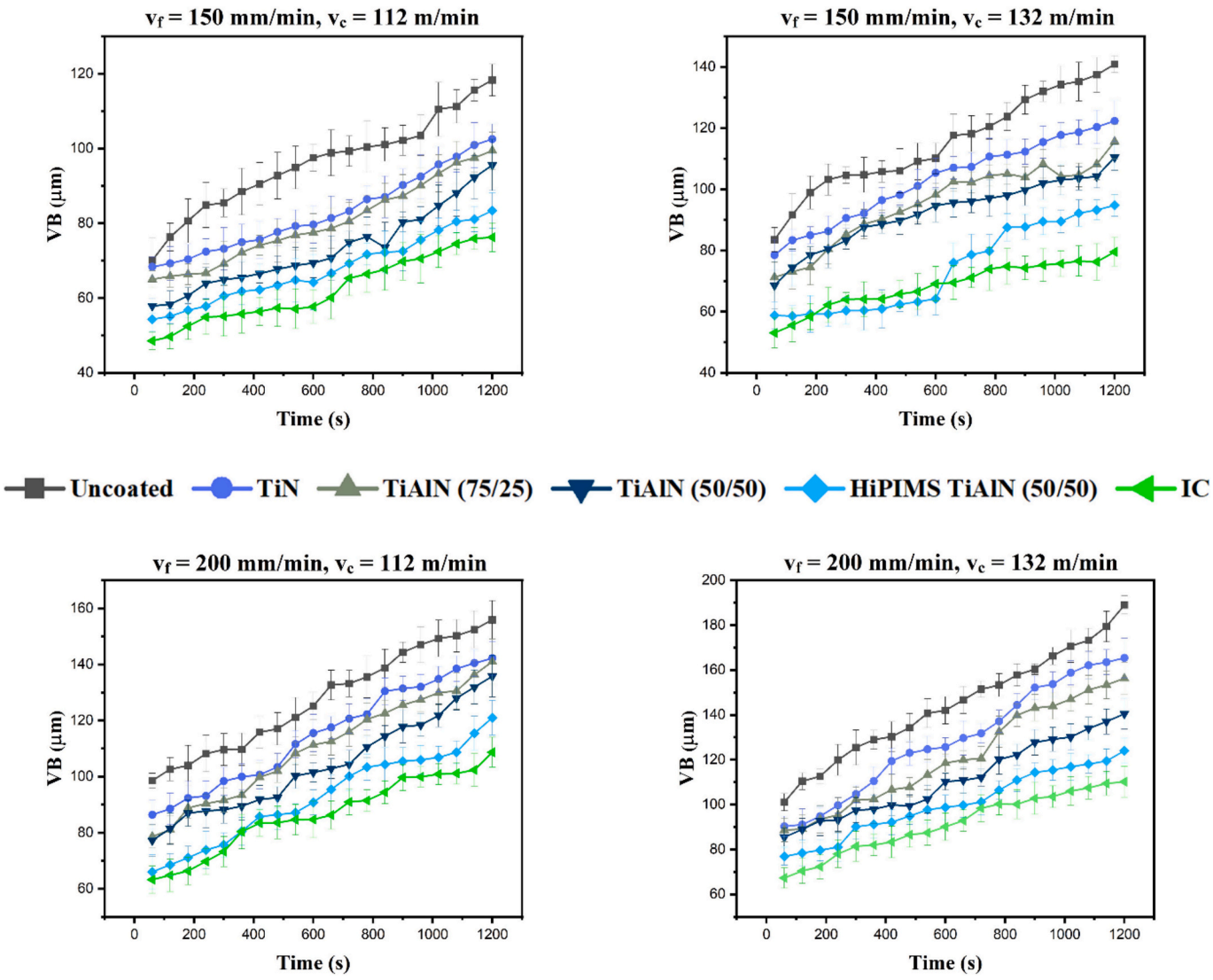


Fig. 4. Flank wear width at flank face for uncoated, and TiN, TiAlN (75/25), TiAlN (50/50), HiPIMS TiAlN (50/50), and IC coated milling tool inserts at various cutting parameters.

coefficient of friction followed by a transition to a more stable regime. This initial increase can be associated with the running-in stage, during which asperity interactions are progressively established and the real contact area between the tribopair increases. Once the contact conditions become more stabilised, a quasi-steady frictional behaviour is attained.

For the uncoated specimen, high fluctuations across tests were recorded at 10 N. This can be attributed to the sensitivity of the line-contact configuration to contact conformity and alignment at low normal load. Under these conditions, the contact may not be fully stabilised during the initial sliding stage, leading to intermittent asperity interactions and uneven load sharing between successive tests. In the absence of a protective coating, these effects are further amplified by direct interaction, which results in a wider scatter band in the coefficient of friction. At higher normal loads, the contact becomes more fully established and mechanically stabilised, thereby reducing test-to-test variation and producing a more consistent friction response.

For the TiN-coated specimens, a more controlled frictional response was obtained at all three loads. After the initial running-in stage, the coefficient of friction was reduced and maintained within a narrower range than that of the uncoated specimen. At 10 N, the TiN coating produces a smoother response with lower fluctuations than the uncoated specimen, indicating that direct interaction between the counterface and the cemented carbide substrate has been effectively suppressed. At 15 N, the behaviour of the coefficient of friction is almost identical across tests, with only minor variations over time. However, at 20 N, the fluctuations of the coefficient of friction across tests increase again. The reason for this will be explained later in this section.

The IC-coated specimens also exhibited improved frictional performance compared with the uncoated condition. At 10 N, a comparatively rapid rise in the friction coefficient is observed during the running-in stage, after which a stable region is established with moderate fluctuations. At 15 N and 20 N, the friction response is slightly more uniform.

When the load was increased from 10 N to 20 N, the overall friction behaviour was not altered drastically, but changes were observed in the intensity of the initial transient and in the extent of fluctuations across tests. Nevertheless, the coated specimens continued to exhibit a more stable frictional response than the uncoated ones, indicating that the coatings provide better interfacial protection and more consistent sliding behaviour. Overall, the friction results confirm that both TiN and IC coatings are effective in improving tribological performance at room temperature, while the uncoated specimen is subjected to more severe and unstable conditions.

As stated earlier in the article, the objective behind developing this

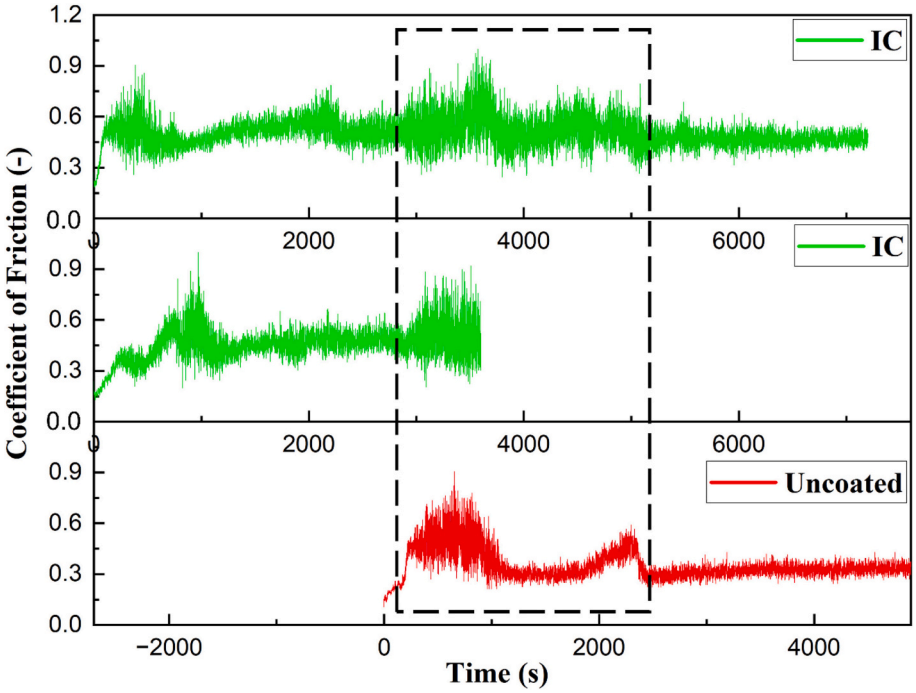


Fig. 5. Variation of the coefficient of friction for IC and uncoated specimens at 5 N load and different test durations.

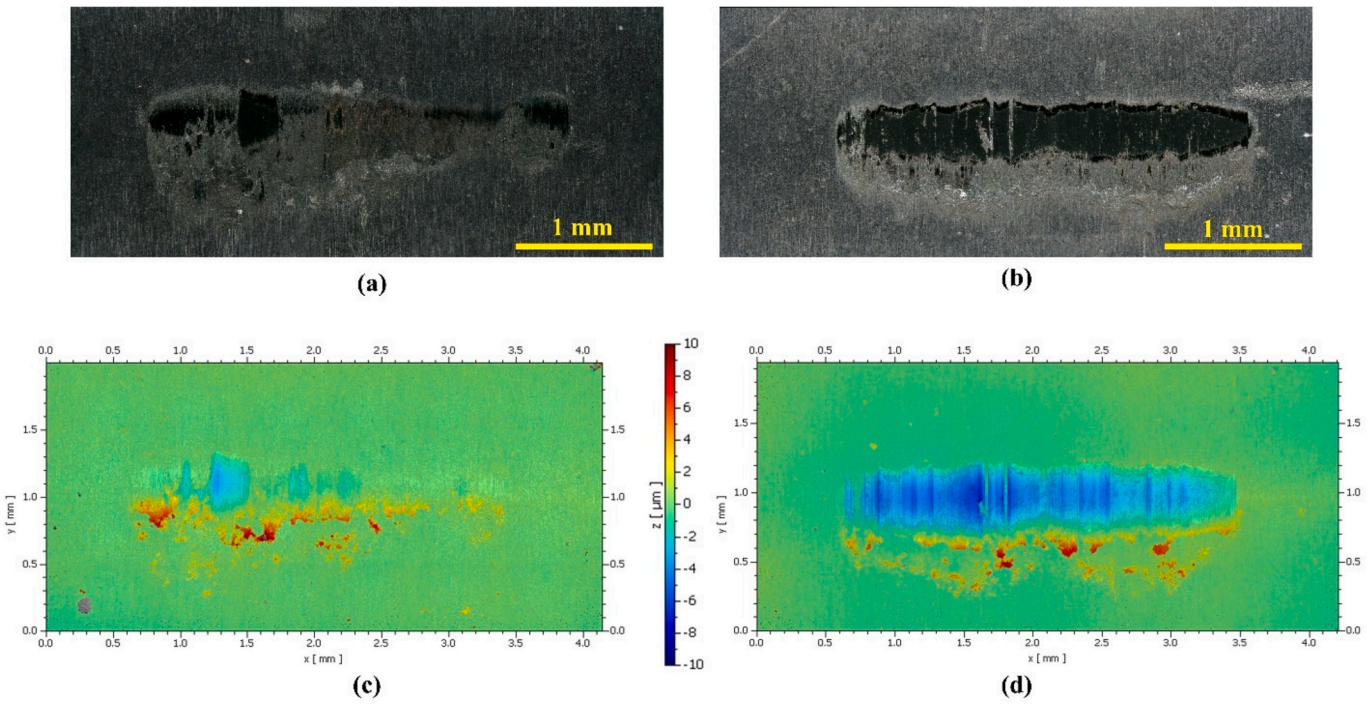


Fig. 6. Light microscopy and optical profilometry images of the wear scar for IC specimen tested at (a), (c) 3600 s, and (b), (d) 7200 s.

model tribological test was to reproduce wear mechanisms similar to those observed during the milling experiments. To verify this similarity, SEM analyses were conducted on the wear scars, and the observed wear features were compared with the wear mechanisms identified in the milling tests. In the milling test, the coating wore out very fast, and it became difficult to analyse the wear mechanisms at play. Therefore, some interrupted milling tests were conducted, during which the milling tool wear was analysed under SEM after each cut.

In the tribological tests of the uncoated specimen, only material removal was observed on the wear scar (Fig. 8 (a)), with some debris from the C45 countersurface. At the edge of the wear scar, the worn cemented carbide surface appeared smoother than the unworn region, suggesting that the asperity peaks were flattened by repeated contact, micro-abrasion, and plastic deformation. Therefore, the wear process involved both severe material removal and polishing-like surface smoothing in the peripheral worn zone. A similar type of surface smoothening was also observed on the milling tools after two milling cuts (Fig. 9). It has been reported that this smooth appearance results

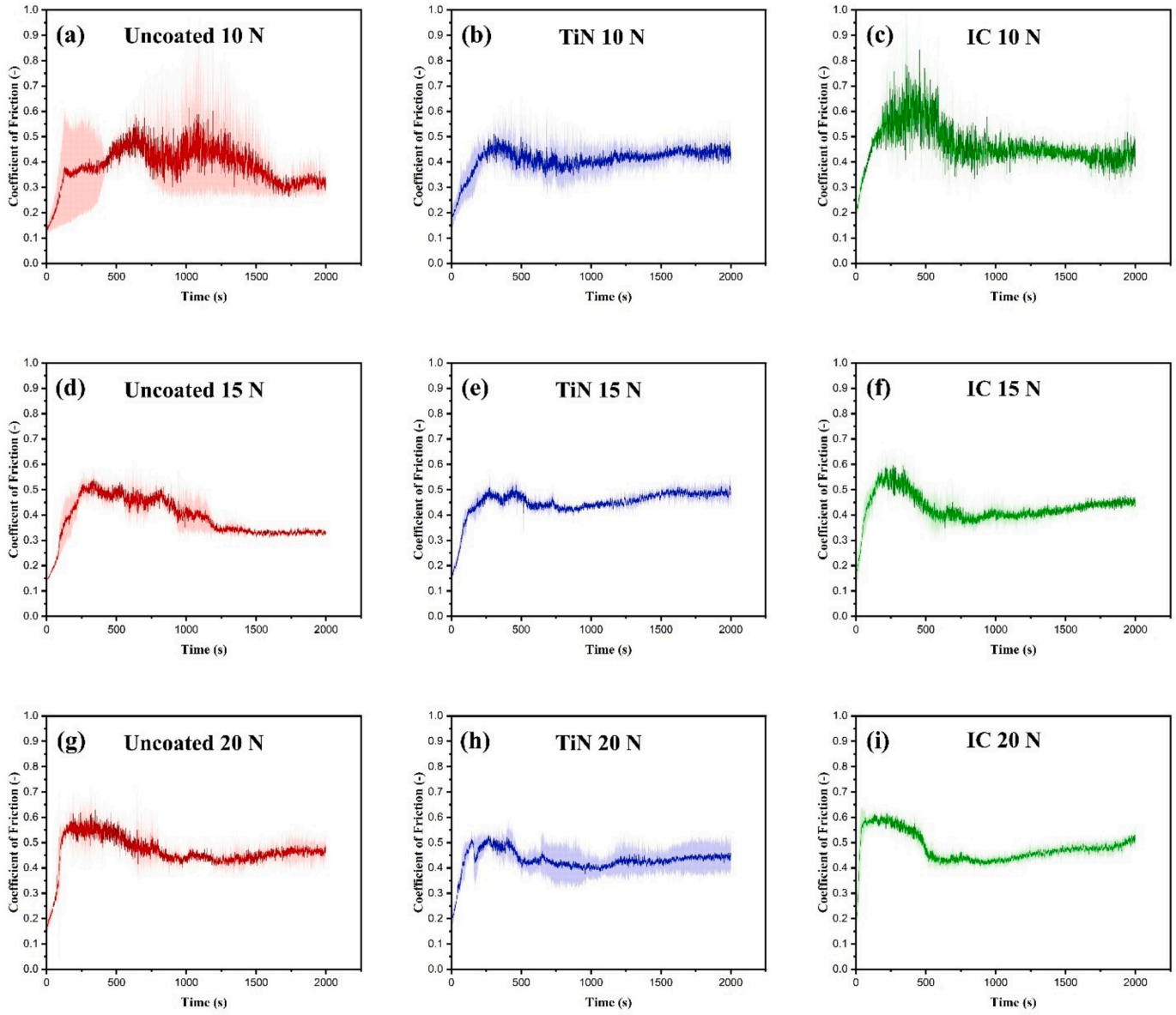


Fig. 7. Variation of the coefficient of friction with time for uncoated, TiN-coated and IC specimens at different normal loads at 25 °C. The dark line is the arithmetic mean of 6 independent repetitions; the semi-transparent band denotes the standard deviation variation across six repetitions.

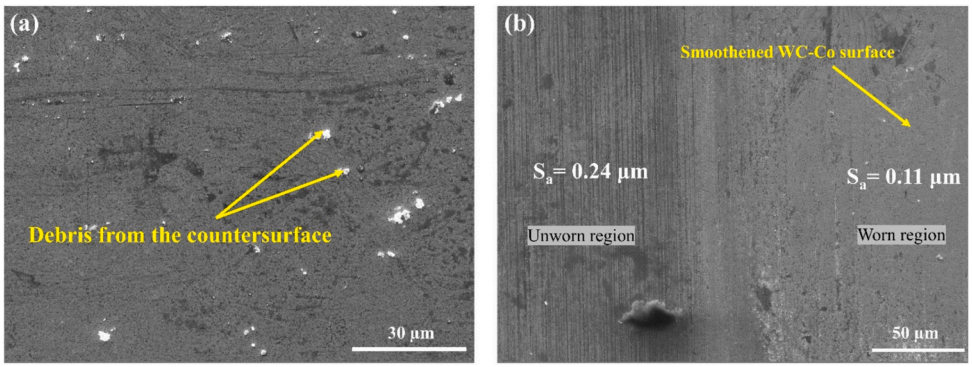


Fig. 8. SEM images of the wear scar of the uncoated specimen tested at 15 N load and 0.25 m/s velocity for 2000 s.

from diffusion wear [48]. Diffusive wear during machining is a thermally activated mechanism in which atoms are transferred between the tool and the workpiece or chip when they come into contact at elevated temperatures [49]. The extent of this wear depends on several factors, including the mutual solubility of the interacting elements, the temperature in the secondary shear zone, the contact pressure, and the

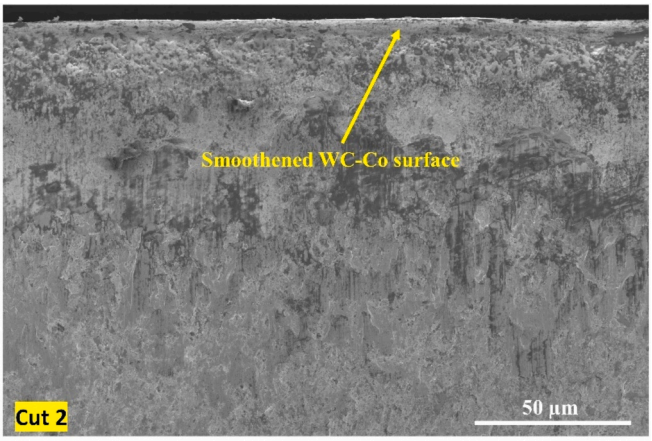


Fig. 9. SEM image of the wear scar on the flank face of the uncoated milling tool after two cuts.

duration of contact [50]. Although the actual contact time between the chip/workpiece and the tool is generally short due to the high cutting speed, diffusion can still occur in localised seizure regions. Since these contact zones are continuously renewed during cutting, saturation is not reached, and the diffusive process can continue throughout machining. In cemented carbide tools, diffusion wear is particularly significant because tungsten carbide and cobalt can interact with hot chips and workpiece material (Fe in C45 has a high affinity for Co in the cemented carbide tool [51]), leading to the selective removal of binder or carbide constituents. At high cutting temperatures, this may weaken the tool surface and accelerate flank wear by changing the local microstructure and reducing the mechanical integrity of the cutting edge. Diffusion wear is generally facilitated by the diffusion of Co from the cemented carbide matrix to the surface. To investigate whether a comparable diffusion-related mechanism occurred during the tribological tests, a FIB cross-section was taken from the central region of the wear scar, and EDX line mapping was carried out to evaluate cobalt distribution in the uncoated specimen (Fig. 10). The Co profile in Fig. 10(b) shows a marked increase in signal intensity close to the surface, after which the intensity decreases toward the interior of the specimen. Such a profile may be interpreted as evidence of near-surface Co enrichment, possibly caused by thermally assisted diffusion during sliding. The presence of additional peaks at greater depth is attributed to the natural occurrence of Co as the binder phase within the cemented carbide microstructure.

The left SEM image in Fig. 11 shows an overview of the wear track on the TiN-coated specimen, where several plastically smeared patches of adhered C45 material are visible along the sliding direction, indicating substantial transfer of counterface material onto the coating. The right, higher-magnification view of the marked region reveals coating chip off due to the transferred material, demonstrating that wear is highly localised and associated with discrete junction formation and rupture rather than uniform abrasion of the coating. The absence of deep grooves or extensive third-body abrasion, together with the presence of these discrete transfer patches, is characteristic of adhesion wear. It has also been reported in the literature that the main governing mechanism for TiN coating is adhesive wear for most of the cutting conditions, and these effects can be attenuated with cutting fluid and cryogenic cutting conditions [52]. Since all the tribological experiments were conducted under unlubricated conditions, adhesive wear had to be the governing mechanism. Similar adhesive wear behaviour was also observed on the TiN-coated milling tools. Fig. 12 presents SEM cross-sections of the TiN-coated cutting edge after the third and fourth milling cuts. In Fig. 12(a), region I indicates the initial transfer of C45 workpiece material onto the TiN coating, forming an adhered layer at the tool-chip interface. As sliding continues, this transferred layer locally drags and partially detaches the TiN, resulting in the mixed region II, which consists of Fe- and O-rich transferred material together with Ti from the coating, as confirmed by the corresponding EDX spectrum. Finally, once the transferred layer has completely removed the coating, the underlying WC–Co substrate becomes exposed, as seen in region III. After the fourth cut, Fig. 12(b) shows that this adhesive transfer layer has fully stripped the TiN in the affected zone, leaving a continuous exposed WC–Co surface and thereby evidencing a progressive, adhesion-driven removal of the coating.

The IC-coated specimen showed a wear behaviour similar to that of the TiN-coated specimen in the tribological tests. Transferred material from C45 countersurface was observed in the wear scar (Fig. 13(a)). Also, when the transferred layer was examined more closely, two distinct regions were observed: one smooth (region I) and the other rough (region II). On examining the different regions with EDX, it was found that the region I comprised mainly of Fe and O atoms, indicating a transferred layer from the C45 countersurface. Whereas region II showed the presence of Ti and Al atoms along with Fe and O. This suggests the wear mechanism was similar to that of the TiN-coated specimen, where the first layer of C45 steel adheres to the coating, and then it takes away some part of the coating through an adhesive wear mechanism. However, this behaviour differed from that reported for TiAlN-based coatings. As the ICs were TiAlN-based coatings, they

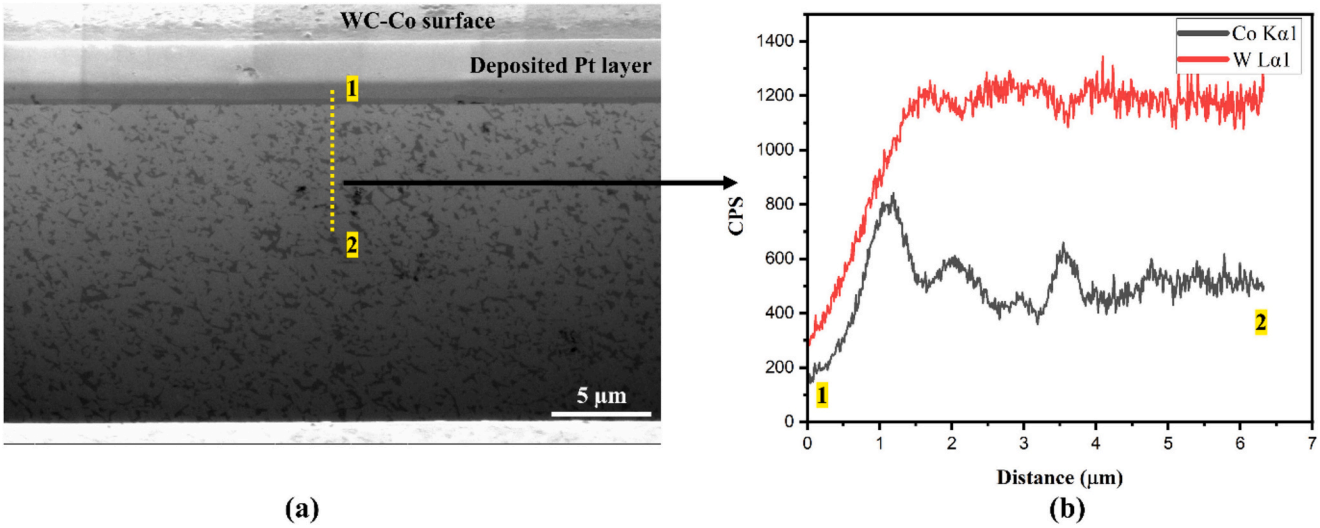


Fig. 10. (a) FIB cross-section image of wear scar from tribological test on uncoated specimen, and (b) EDX line scan from the top of the FIB cross-section.

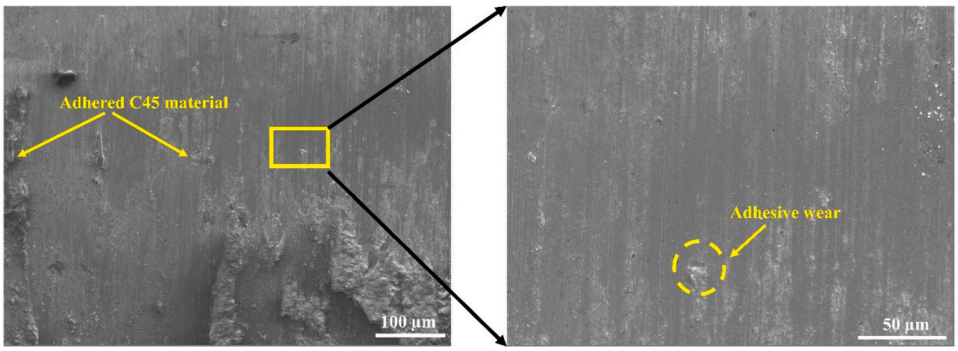


Fig. 11. SEM image of wear scar of TiN-coated specimen tested at 15 N load and 0.25 m/s speed for 2000s.

should have been less prone to adhesive wear because of the presence of aluminium. The presence of aluminium increases the thermal stability of the coatings, and at milling temperatures, Al-rich oxides (Al_2O_3 mixed with TiO_2/Fe-oxides) form a chemically more inert, ceramic-like interlayer between chip and coating, which lowers the tendency for Fe—Ti metallic bonding, and acts as a diffusion barrier against Fe and C penetration [53]. When the wear of the IC-coated milling tool was analysed after 1, 2, 3, and 4 cuts (Fig. 14), the results agreed with those reported in the literature. Adhesion was not the dominant wear mechanism, as in the TiN-coated specimen (Fig. 12), where a prominent transferred layer was observed. The wear mechanism of the IC-coated milling tool was predominantly abrasive, with only minor signs of adhesive wear.

Specific wear rates of the wear scars from the tribological tests were measured and plotted for various specimens at different loads at 25 °C (Fig. 15(a)). At 10 N load, there is little difference in the specific wear rates between the uncoated and coated specimens. At 15 N load, the specific wear rate of the uncoated specimen could be differentiated from the specific wear rates of the coated specimens. Still, the difference in specific wear rates between coated specimens was not large enough to place other coatings between them. At 20 N, however, the apparent specific wear rate of the TiN-coated specimen cannot be reliably quantified because of pronounced material transfer from the C45 counterpart. As shown by the FIB cross-section in Fig. 15(b), the transferred layer extends through the entire TiN coating thickness and reaches the coating–substrate interface, making it impossible to separate true coating removal from adhered C45 material when calculating the wear volume. The strong fluctuations in the coefficient of friction recorded for the TiN-coated specimen at 20 N (Fig. 7(h)) are consistent with this observation and can be attributed to the highly non-uniform build-up and disruption of the transferred layer within the tribological contact across various repetitions. The similar specific wear rate of the coated specimens might have resulted from the similar wear mechanisms at play during the tribological tests. Generally, with TiAlN-based coatings, the formation of Al_2O_3 plays an important role in preventing damage from adhesive wear. There is a high possibility that during the tribological tests at 25 °C, sufficient thermal activation energy was not provided to the coating, which would have facilitated the formation of Al_2O_3. Since the authors had no information on the composition of the IC-coated specimen, TiAlN (75/25)-coated specimens were introduced into the tribological tests, and they also exhibited similar behaviour. The room-temperature tests were conducted for all coatings and revealed no significant differences in wear volume; this absence of differentiation prompted the elevation of test temperature to 100 °C. Therefore, moving forward, a 15 N load was chosen as the most suitable load within the tested range, as the wear volume was easier to quantify across all coatings, and the testing temperature was increased to 100 °C.

For the uncoated specimen, the 100 °C tests produced a compacted, mechanically mixed transfer layer on the C45 counterface. We attribute its formation to third-body compaction of WC-rich debris detached from the cemented carbide and partially oxidised in ambient air; its formation is promoted at 100 °C by thermally assisted Co depletion of the near-surface binder phase, for which the Co profile in Fig. 10(b) provides independent evidence. Crucially, this layer is retained in the tribotest because the closed, unidirectional ring track is re-traversed continuously and third bodies accumulate, whereas in milling, the chip and the workpiece surface are continuously renewed and no comparable layer can establish itself. The uncoated tribotest therefore experiences an artificial protective effect that has no counterpart in the milling contact, and the resulting wear mechanisms are not representative of an unprotected tool. For this reason, the uncoated specific wear rate value is excluded from the modelling, while the mechanistic observations obtained on the uncoated specimen (Figs. 8–10) are retained, since they are unaffected by this artefact. Obtaining a valid unprotected baseline would require a contact configuration with a continuously renewed counterface, such as a single-pass or spiral sliding path, which we identify as a subject for future work. As a consequence, the grey-box model presented here is restricted to coated tools, and the uncoated milling data in Fig. 4 serve as an experimental reference rather than as a model input. The specific wear rates of different coated specimens tested at 100 °C showed interesting trends (Fig. 16). As the tribological test temperature increased, a clear distinction emerged in the specific wear rates of the different coated specimens. The TiN-coated specimens showed the highest wear rates, whereas the IC-coated specimens showed the lowest. Also, we observed the influence of the elemental composition on the wear behaviour of TiAlN-based coatings. Among the in-house-grown coatings, TiAlN (50/50)-coated specimens showed the lowest specific wear rate. Staia et al. [54] also reported that an intermediate composition of Al around $x \approx 0.5$ in the $Ti_xAl_{1-x}N$ structure suppresses adhesive wear more effectively than other compositions. Knotek et al. [19] also identified diffusion wear as a major cutting-tool wear mechanism and gave the mechanistic rationale for adding Al to Ti-based nitrides in the first place: the resulting Al_2O_3 top layer suppresses diffusion into/out of the coating. Hence, the tribological tests captured the influence of elemental effects on the coatings. Fig. 17 shows the SEM images of the wear scar for TiN and TiAlN (75/25) specimens at 25 °C and 100 °C. It was observed that the wear mechanism in the case of the TiN-coated specimen remained dominated by adhesive and abrasive wear at 100 °C, whereas in the TiAlN (75/25)- coated specimen, it was mostly abrasive wear. This can be attributed to the formation of Al_2O_3 on the surface, which reduces adhesion [19,53,54]. This is consistent with pin-on-disk studies on (Ti,Al)N/γ-Al_2O_3 systems, where the γ-Al_2O_3 top layer reduced the wear rate by nearly an order of magnitude at 600–800 °C compared with plain (Ti,Al)N [8].One important thing to note here is that although the testing temperature of 100 °C is not very high, it still leads to the formation of Al_2O_3 as the temperature at the contact zone, i.e., the flash temperature, is always way higher than the ambient temperature. However, future work will include a detailed investigation of this Al_2O_3 layer with Raman and XPS measurements. Additionally, the HiPIMS TiAlN (50/50)-coated specimen exhibited a

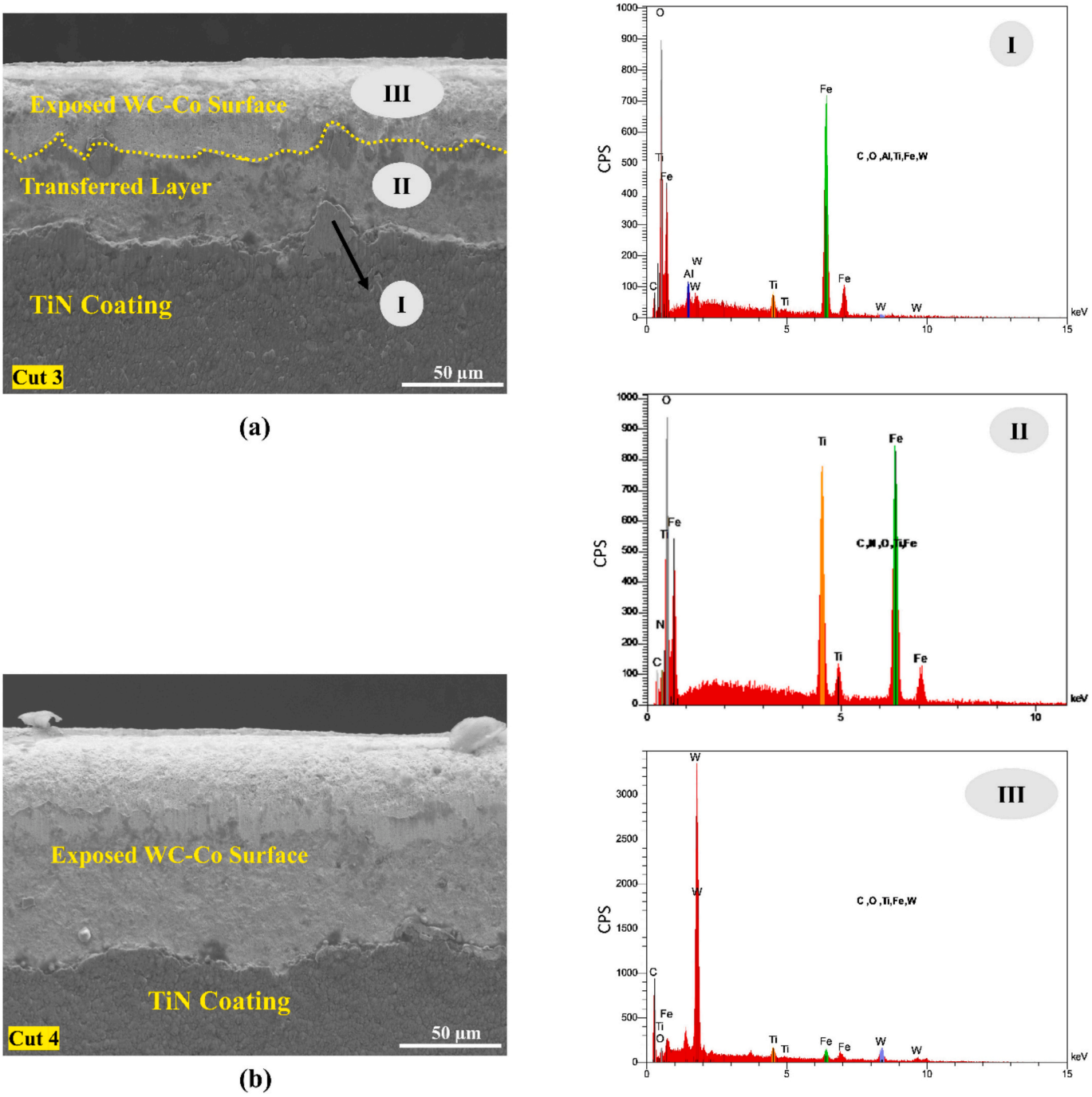


Fig. 12. SEM images of milling tool after (a) 3 cuts, and (b) 4 cuts, along with the EDX spectra of various regions in the SEM image after 3 cuts. The coloured peaks in EDX spectra are element identification markers automatically generated by the analysis software.

lower specific wear rate than the conventionally DC-magnetron sputtered TiAlN (50/50) coating, even though both coatings had similar Ti/Al ratio. This improvement can be attributed to the denser, finer-grained microstructure (Fig. 2(c) and (d)) produced by the HIPIMS process, which reduces defect density and enhances the load-bearing capacity of the coating, thereby suppressing wear and crack initiation under sliding contact. This result is consistent with reports that ion-bombardment-driven densification and grain refinement improve the wear resistance of Ti-Al-N coatings [44]. Moreover, the relative ranking of the coatings obtained in the tribological tests was the same as observed in the milling tests at different cutting parameters (Fig. 4). It must be noted that the 2000s duration was established on the IC specimen at 5 N and at 25 °C, whereas the evaluation tests were subsequently performed at 15 N and 100 °C; the breakthrough time observed at 5 N therefore does not by itself guarantee coating integrity for the full 2000 s at the higher load. To verify that the calculated specific wear rates are free of substrate contribution for every coating, the maximum wear-scar depth measured by optical profilometry at 15 N and 100 °C is compared with the corresponding coating thickness in Table 1. For all coatings the maximum wear depth remained below coating thickness. However, for the TiN coating, a minor substrate contribution to the measured wear volume cannot be excluded, as is also evident in Fig. 17(b), where the adhesive wear marks actually represent the substrate surface. A decision matrix is also presented in Table 2, which summarises the criteria for parameter selection for the model tribological test.

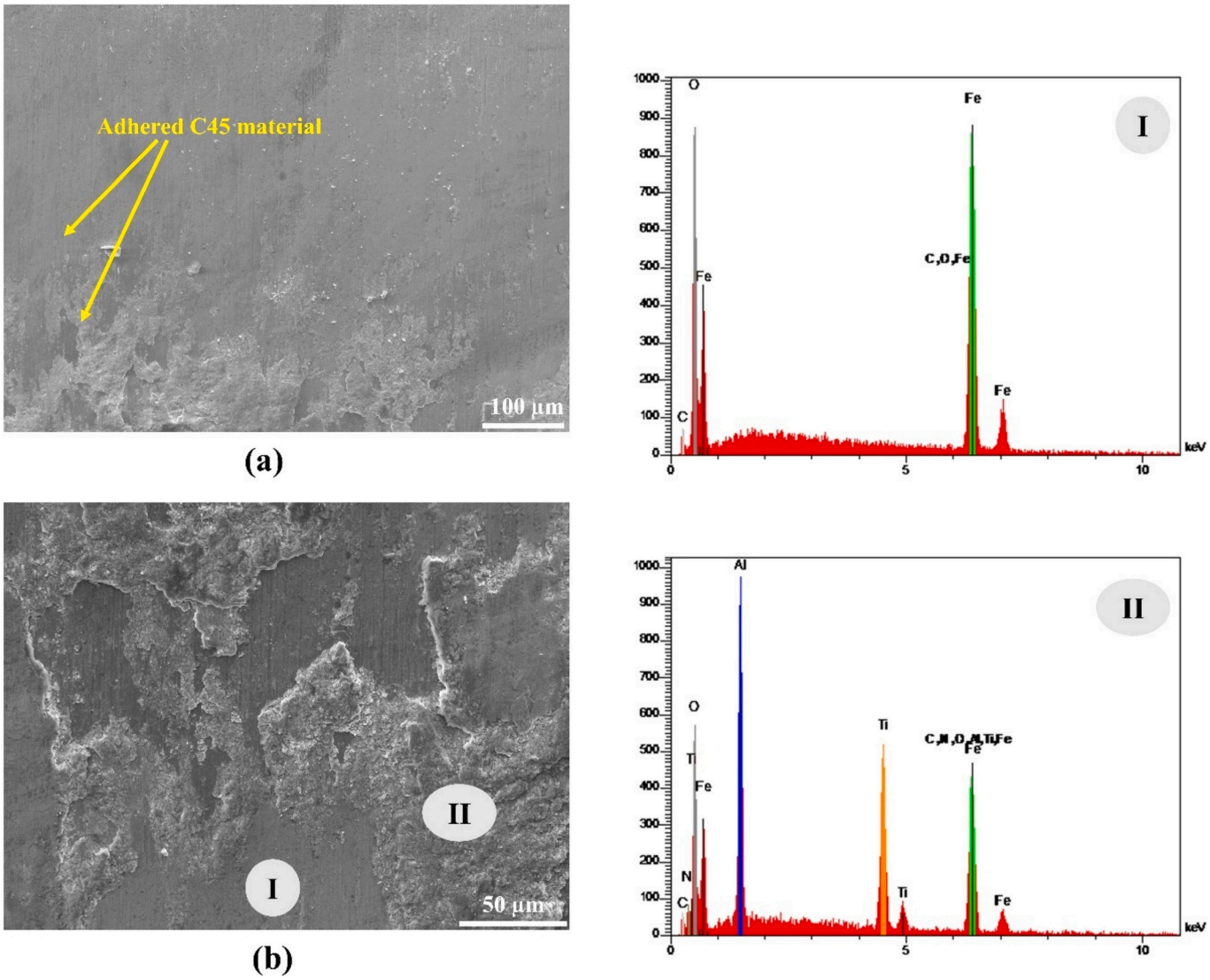


Fig. 13. SEM image of wear scar of IC-coated specimen at different magnifications with the respective EDX spectra of the assigned regions.

3.4. Grey-box modelling for tool wear prediction

After attaining a set of the most suitable parameters within the tested range for the tribological model tests, which can be used to compare the tribological performance of various coatings through the specific wear rate. This specific wear rate was used along with the data of the milling test to create a grey-box model for tool wear prediction in milling operations. The specific wear rate enters the grey-box model as a single scalar per coating, determined at one reference condition (15 N, 100 °C, 0.25 m/s), and is treated as invariant with respect to contact pressure, temperature and sliding velocity. The specific wear rate was not used as an Archard wear coefficient, but as a coating-identifying feature, while the process dependence of wear in milling is carried by the cutting parameters and by the simulated interface temperature, sliding velocity and normal stress. The model, therefore, does not require the specific wear rate to be numerically transferable to milling conditions; it requires only that the specific wear rate be monotonic in the intrinsic wear resistance of the coatings across the set considered, which the agreement between the tribotest ranking and the milling ranking confirms for the present material window. In our earlier study [39], we established a grey-box framework that links coating-specific tribological behaviour to time-dependent tool wear in milling by means of a process-tribology descriptor. The approach combines (i) machining experiments, providing VB as a function of cutting speed, feed and time, (ii) simplified tribological model tests on coated WC-Co cylinders against C45 steel (through the testing route discussed in the present manuscript), and (iii) thermo-mechanical quantities from white-box chip-formation simulations (maximum interface temperature, sliding velocity and normal stress). From the tribological tests, a coating-specific wear parameter (Ws) is extracted as the specific wear rate, which compactly characterises the intrinsic wear resistance of each coating under a well-defined contact configuration.

This descriptor Ws is then embedded into a data-driven wear law: a black-box model first uses v_c, v_f, time (t) and Ws to capture the dominant trend of flank-wear evolution, after which a physics-informed grey-box model refines the prediction by additionally incorporating the simulated thermo-mechanical fields. Importantly, this grey-box model was evaluated in an extrapolative setting rather than by interpolation: the coating whose milling wear behaviour was to be predicted was deliberately omitted from the training data, and the model inferred its response solely from the tribological descriptor Ws together with the simulated thermo-mechanical fields. This design highlighted the central role of the tribological tests. The specific wear rate obtained from the model tribological tests served as a transferable descriptor, enabling reliable tool-wear prediction for coatings not encountered during training, thereby demonstrating how targeted tribological characterisation can

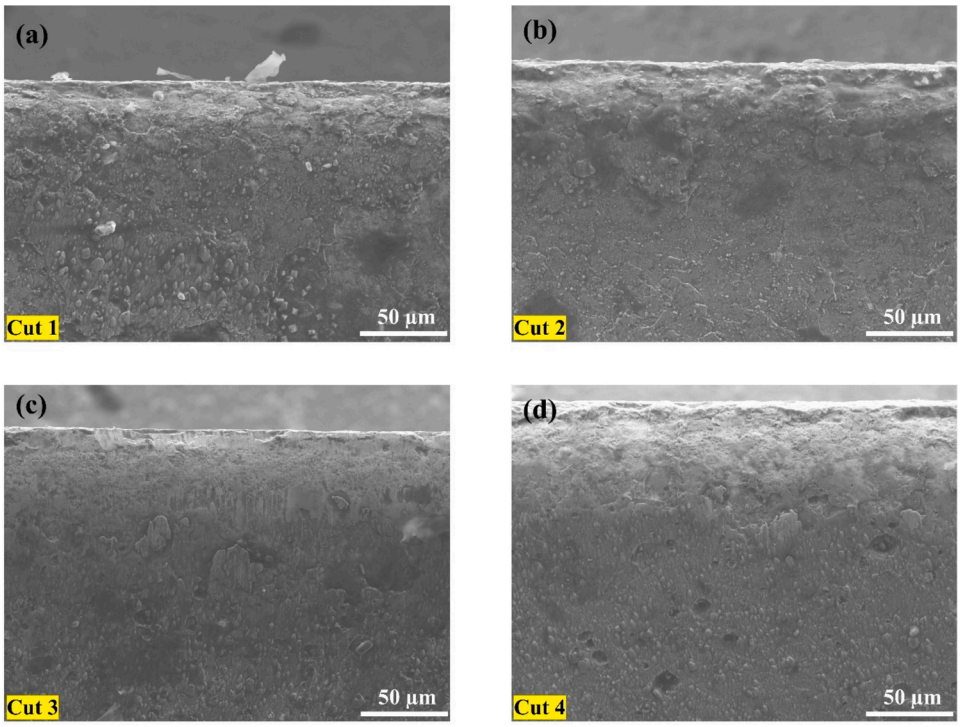


Fig. 14. SEM images of IC-coated milling tools after (a) 1, (b) 2, (c) 3, and (d) 4 cuts showing abrasion as the most dominant wear mechanism.

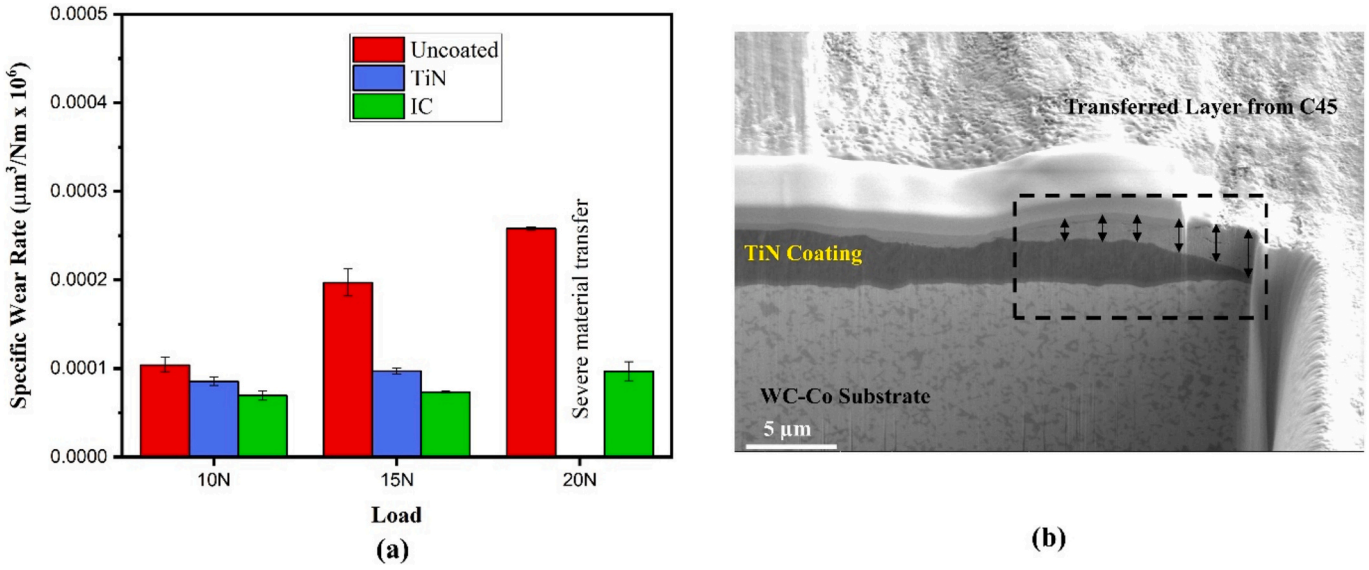


Fig. 15. (a) Specific wear rates of different coated specimens in tribological tests under different loads and at 25 °C; (b) FIB cross-section of TiN-coated specimen under tribological test at 20 N load showing the extent of the transferred layer till the thickness of the TiN coating.

close the gap between coating-scale behaviour and machining-scale wear evolution. For a full description of the workflow and model formulation, readers are referred to Jamali et al. [38,39].

Table 3 summarises the predictive performance (flank wear) of the black-box and grey-box wear models for all investigated coatings and cutting conditions. Across all combinations of v_c and v_f, the grey-box consistently yields higher R^2 values and lower RMSE than the purely data-driven black-box model, indicating both a better reproduction of the time-dependent flank-wear evolution and a smaller absolute prediction error. At the lower cutting speeds, where the wear evolution is close to linear, and the simulated thermo-mechanical fields vary least, so that the additional physics-based inputs contribute least discriminating information, and the more flexible black-box model can fit the data marginally more closely, the two lowest black-box RMSE values of the entire matrix occur precisely under these conditions. The advantage of grey-box becomes particularly pronounced at the highest v_c-v_f combinations, where the R^2 of the black-box model drops markedly while the grey-box still maintains high R^2, and RMSE values in the low micrometre range. The reduced robustness of the black-box model at high cutting speeds and feeds can be attributed to stronger non-linearities and extrapolation in the underlying wear behaviour, which are difficult to capture from machining data alone. In contrast, the grey-box approach is not constrained by the process-tribology descriptor (Ws) only; it also has physics-based thermo-mechanical inputs (interface temperature,

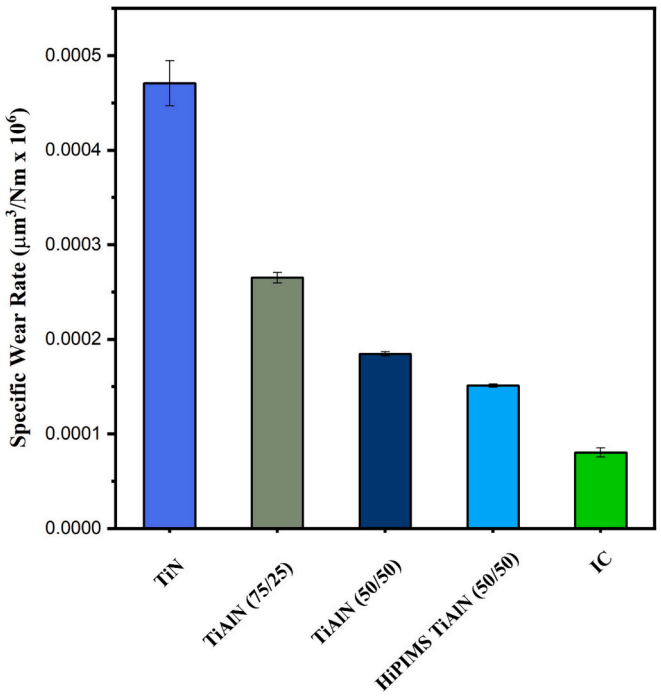


Fig. 16. Specific wear rates of different coated specimens tested at 15 N, 0,25 m/s and 100 °C for 2000 s [39].

sliding velocity and normal stress), so that the model structure not only encodes the dominant wear-driving mechanisms but also remains reliable even when the operating point moves toward more severe machining conditions.

3.5. Limits of transferability of the model tribotest

The model tribotest employed in this work deliberately trades process fidelity for throughput and control, and two differences from the milling contact must be stated explicitly. First, the ring-on-cylinder configuration imposes continuous unidirectional sliding, whereas milling is an interrupted process in which the coating experiences cyclic mechanical impact and thermal cycling at every tooth engagement. Coating failure modes driven by cyclic loading, interfacial fatigue, delamination, and edge chipping are therefore not activated in the model test, and the descriptor Ws carries no information about impact-fatigue resistance. Second, the quasi-steady thermal state of the tribotest does not reproduce the repeated formation and spallation of protective oxide layers that occur under interrupted cutting. Accordingly, the framework proposed here should be understood as a screening and ranking method for the steady-state, mechanism-driven component of coating wear, not as a quantitative emulation of the milling contact. Its transferability is expected to be good for coating sets whose relative performance is governed by composition- and microstructure-controlled abrasion and adhesion resistance, as demonstrated here.

Direct attribution of the improved wear resistance of the DCMS- and HiPIMS-deposited TiAlN (50/50) coatings to their deposition-related microstructure alone is not possible, since the two coatings differ simultaneously in thickness (5.5 μm and 2.1 μm) and in growth

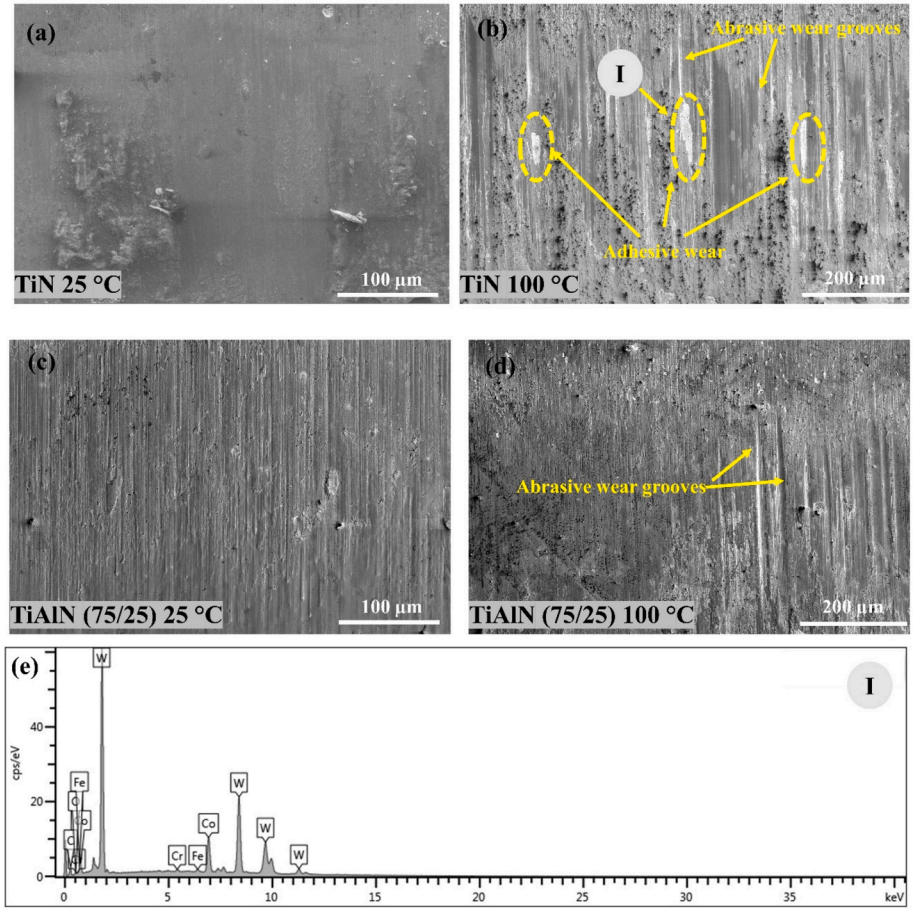


Fig. 17. (a,b,c,d)SEM images of the wear scar of TiN and TiAlN (75/25)- coated specimens at 25 °C and 100 °C, and (e) EDX spectrum of adhesive wear scar shown in (b) depicting the substrate exposure.

Table 2
Parameter selection criteria for the model tribological tests.

Criterion	Metric used	10 N	15 N	20 N
Wear discrimination	Specific wear rate ratio (TiN / IC); separation exceeding combined scatter	Insufficient, uncoated and coated indistinguishable (Fig. 15(a))	Sufficient, uncoated separated from coated; coating ranking resolved at 100 °C (Fig. 16)	Not assessable for TiN
Measurement reliability	Wear volume quantifiable for all five coatings	Yes, but within scatter	Yes, for all coatings	No, the transferred layer reaches the interface on TiN (Fig. 15(b))
Contact stability	Test-to-test scatter band of the coefficient of friction over 6 repetitions	Large scatter, unstable line contact at low load	Smallest scatter; coefficient of friction nearly identical across repetitions	Scatter increases again due to non-uniform transfer layer build-up (Fig. 7(h))
Coating integrity	Maximum wear scar depth at 2000 s	Well within coating	Within coating for all coatings (Table 1)	Interface reached for TiN
Outcome		Rejected, no discrimination	Selected	Rejected, measurement artefact

Table 3
Summary of prediction performance of flank wear for various coatings at different milling parameters.

v_c (m/min)	v_f (mm/min)	Coatings	R^2 (Black-Box)	RMSE (μm) (Black-Box)	R^2 (Grey-Box)	RMSE (μm) (Grey-Box)
112	150	TiN	0.91	1.42	0.941	1.98
		TiAlN (75/25)	0.882	3.67	0.909	3.22
		TiAlN (50/50)	0.882	3.67	0.892	3.51
		HiPIMS TiAlN (50/50)	0.895	2.83	0.911	2.61
		IC	0.884	2.51	0.927	2.01
112	200	TiN	0.891	4.27	0.911	3.93
		TiAlN (75/25)	0.852	6.41	0.942	3.43
		TiAlN (50/50)	0.902	2.16	0.918	4.86
		HiPIMS TiAlN (50/50)	0.873	5.7	0.923	3.18
		IC	0.887	4.83	0.916	3.87
132	150	TiN	0.915	3.84	0.943	2.27
		TiAlN (75/25)	0.824	5.29	0.914	3.95
		TiAlN (50/50)	0.831	5.02	0.919	3.41
		HiPIMS TiAlN (50/50)	0.836	4.63	0.938	2.57
		IC	0.841	4.29	0.947	2.18
132	200	TiN	0.823	7.31	0.927	3.22
		TiAlN (75/25)	0.888	3.48	0.938	3.01
		TiAlN (50/50)	0.864	4.01	0.946	2.94
		HiPIMS TiAlN (50/50)	0.797	10.53	0.921	3.26
		IC	0.806	8.93	0.948	2.03

morphology. A thickness-matched HiPIMS coatings would be required to isolate the microstructural contribution unambiguously. Also, both the tribotest and the grey-box model were calibrated exclusively on monolithic TiN and $Ti_{1-x}Al_xN$ coatings sliding against normalised C45 steel, and the extrapolative capability demonstrated by the leave-one-coating-out validation is therefore established only within this material window. The decisive requirement for generalisation is not chemical similarity as such, but that Ws remain rank-preserving with respect to the mechanism that differentiates the coatings under consideration. On this basis, transfer to further monolithic ternary nitrides whose performance is governed by composition-controlled abrasion and oxide passivation appears plausible, and quaternary Ti-Si-Al-N coatings may also remain within reach, although the elevated activation temperature of the amorphous Si_3N_4 phase lies above the present tribotest window. In contrast, multilayer, nano-multilayer and composition-graded architectures are not expected to be captured without adaptation: their wear resistance is governed by interface-driven crack deflection and cyclic-load-bearing capacity, which the continuous-sliding contact of the model test does not activate, and a single scalar descriptor is not well defined for a depth-varying architecture. Extending the framework to these systems will require both an intermittent, impact-loaded tribotest variant and a layer-resolved or depth-weighted effective wear descriptor.

4. Conclusions

This study demonstrates that carefully designed model tribological tests can provide a reliable and efficient basis for evaluating cutting tool coatings and predicting their wear behaviour in milling. By tuning the ring-on-cylinder conditions to a load of 15 N, a sliding speed of 0.25 m/s and a test temperature of 100 °C, short-duration tests of 2000 s yielded specific wear rates that clearly discriminated between TiN, TiAlN (75/25), TiAlN (50/50), HiPIMS TiAlN (50/50) and an IC. The resulting coating hierarchy for the highest specific wear rate: TiN ≫ TiAlN(75/25) > TiAlN (50/50) > HiPIMS TiAlN (50/50) > IC, was identical to the ranking obtained from flank-wear evolution in milling, indicating that the tribotest captures the essential coating-dependent wear response despite its greatly reduced complexity and duration.

Beyond reproducing the global ranking, the tribological framework was sensitive to both elemental and microstructural differences in the TiAlN system. The specific wear rate revealed the beneficial effect of Al addition, with lower wear in TiAlN than in TiN, and further distinguished between TiAlN (50/50) and HiPIMS TiAlN (50/50), which have nominally identical Ti/Al ratios but markedly different microstructures. The lower specific wear rate of the HIP TiAlN (50/50) coating reflects its finer and denser columnar morphology, demonstrating that the model test responds not only to chemistry but also to subtle changes in coating architecture. SEM and FIB/EDX analyses confirmed that the selected tribological contact conditions reproduce the dominant wear mechanisms observed in milling, diffusion-assisted smoothing for the uncoated substrate, adhesion-dominated transfer and coating pull-off for TiN, and predominantly abrasive wear for Al-rich TiAlN, thereby supporting the use of the specific wear rate from tribological tests as a mechanistically meaningful descriptor rather than a purely empirical metric.

Within the grey-box modelling framework, the specific wear rate (W_s) obtained from tribological model test serves as a coating-specific process-tribology descriptor that links coating-scale behaviour to milling-scale flank wear. Embedded into a data-driven wear law together with cutting parameters and thermo-mechanical fields from chip-formation simulations, W_s enabled accurate prediction of tool wear for all investigated coatings and cutting conditions and, crucially, allowed extrapolative assessment of an unseen TiAlN coating that was excluded from the training set. Across all v_c-v_f combinations, the grey-box model achieved higher coefficients of determination and lower

RMSE than a purely data-driven black-box model, with the performance gap increasing at the highest cutting speed and feed, where non-linear wear behaviour and limited machining data make black-box extrapolation particularly fragile.

Despite these promising results, the present framework still has some limitations. The results demonstrate that both the specific wear rate descriptor and the proposed grey-box model capture specific features of the investigated coatings, including their composition and structural characteristics, in a generalised form suitable for wear prediction in comparatively simple model cutting processes. Models of higher resolution, supported by a substantially larger database, are nevertheless required to resolve individual coating features quantitatively, in particular the correlation of coating thickness and growth morphology with the wear behaviour, and ultimately to extend the approach to multilayer coating architectures for cutting tools, including modified substrate surface zones and interface layers. Both the tribological tests and the grey-box model were calibrated exclusively for monolithic TiN and TiAlN coatings sliding against normalised C45 steel, and their validity cannot be assumed a priori for other coating chemistries, substrates, or workpiece materials. Furthermore, only monolithic coatings were considered, whereas industrial tools frequently employ multilayer, nano-multilayer or graded architectures whose wear resistance is governed by additional interface-driven mechanisms not yet captured in the current tribotest design or modelling strategy. Future work should therefore establish adapted model tribotests for multilayer and composition-graded Ti-based coatings and explore whether suitably defined layer-resolved or effective wear descriptors can be integrated into an extended grey-box framework. Moreover, the model tribotests also need to account for thermo-mechanical cycling present in milling operations. Finally, the study shows that severe but moderate-temperature laboratory tests (here, 100 °C bulk temperature) are sufficient to activate Al_2O_3-based protection in TiAlN and to resolve coating trends relevant to milling, avoiding the need for extremely harsh oxidation or very high-temperature tribological conditions that have dominated earlier work. Overall, the proposed methodology provides a physically interpretable route from laboratory tribology to machining-scale wear prediction and offers a foundation for future, more general frameworks that incorporate multilayer architectures, additional material systems and broader machining conditions.

CRediT authorship contribution statement

Amod Kashyap: Writing – review & editing, Writing – original draft, Methodology, Investigation, Formal analysis, Data curation. **Amirmohammad Jamali:** Writing – review & editing, Software, Formal analysis, Data curation. **Finn Rümenapf:** Visualization, Formal analysis. **Nelson Filipe Lopes Dias:** Writing – review & editing, Visualization, Formal analysis. **Vincent Ott:** Writing – review & editing, Software, Investigation, Formal analysis. **Wolfgang Tillmann:** Validation, Supervision, Resources. **Michael Stueber:** Writing – review & editing, Visualization, Validation, Supervision, Resources, Project administration, Funding acquisition, Conceptualization. **Johannes Schneider:** Writing – review & editing, Visualization, Supervision, Resources, Project administration, Funding acquisition, Conceptualization. **Volker Schulze:** Writing – review & editing, Validation, Supervision, Resources, Project administration, Funding acquisition, Conceptualization.

Declaration of Generative AI and AI-assisted technologies in the writing process

During the preparation of this work the author(s) used DeepL in order to fix the grammatical mistakes and improve the readability of the manuscript. After using this tool/service, the author(s) reviewed and edited the content as needed and take(s) full responsibility for the content of the publication.

Declaration of competing interest

The authors declare that they have no known competing financial interests or personal relationships that could have appeared to influence the work reported in this paper.

Acknowledgements

The authors appreciate the funding of this work within the priority program 2402 “Greybox models for the qualification of coated tools for high-performance cutting” by the German Research Foundation (DFG).

Data availability

Data will be made available on request.

References

[1] E. Segebade, J. Schneider, V. Schulze, Tribological effects in and by metal cutting, in: Key Eng. Mater, Trans Tech Publications Ltd, 2018, pp. 3–24, https://doi.org/10.4028/www.scientific.net/KEM.767.3.
[2] V. Schulze, J. Michna, F. Zanger, C. Faltin, U. Maas, J. Schneider, Influence of Cutting Parameters, Tool Coatings and Friction on the Process Heat in Cutting Processes and Phase Transformations in Workpiece Surface Layers, 2013, https://doi.org/10.3139/105.110177/html.
[3] A. Inspektor, P.A. Salvador, Architecture of PVD coatings for metalcutting applications: a review, Surf. Coat. Technol. 257 (2014) 138–153, https://doi.org/10.1016/j.surfcoat.2014.08.068.
[4] A. Drnovšek, P. Šumandl, Ž. Gostenčnik, J. Kovač, M. Čekada, Cathodic arc-deposited AlTiN hard coating tribology at elevated temperatures, Surf. Coat. Technol. 515 (2025) 132662, https://doi.org/10.1016/j.surfcoat.2025.132662.
[5] V. Terek, L. Kovačević, A. Drnovšek, P. Panjan, B. Škorić, J. Kovač, Z. Bobić, P. Terek, High-temperature tribological behavior of nanolayered TiAlN/TiSiN coating deposited on WC-Co cemented carbide, Surf. Coat. Technol. 477 (2024) 130316, https://doi.org/10.1016/j.surfcoat.2023.130316.
[6] S.J. Bull, D.G. Bhat, M.H. Staia, Properties and performance of commercial TiCN coatings. Part 2: tribological performance, Surf. Coat. Technol. 163–164 (2003) 507–514, https://doi.org/10.1016/S0257-8972(02)00651-5.
[7] H.Y. Li, H.B. He, W.Q. Han, J. Yang, T. Gu, Y. ming Li, S.K. Lyu, A study on cutting and tribology performances of TiN and TiAlN coated tools, Int. J. Precis. Eng. Manuf. 16 (2015) 781–786, https://doi.org/10.1007/s12541-015-0103-4.
[8] K. Bobzin, N. Bagcivan, M. Ewering, R.H. Brugnara, S. Basturk, Comparison of (Ti, Al)N and (Ti,Al)N/γ-Al_2O_3 coatings regarding tribological behavior and machining performance, Surf. Coat. Technol. 257 (2014) 58–62, https://doi.org/10.1016/j.surfcoat.2014.08.070.
[9] F. Attar, T. Johannesson, Adhesion evaluation of thin ceramic coatings on tool steel using the scratch testing technique, Surf. Coat. Technol. 78 (1996) 87–102, https://doi.org/10.1016/0257-8972(94)02396-4.
[10] J. Golden, G.W. Rowe, A simple apparatus for studying the wear of tungsten carbide, Wear 1 (1958) 491–498, https://doi.org/10.1016/0043-1648(58)90517-9.
[11] K. Tijnshoff, A. Mohlfelda, T. Leyendeckerb, H.G. Fulsb, G. Erkensb, R. Wenkeb, T. Csellec, M. Schwenckc, Wear mechanisms of (Til-,Al,)N coatings in dry drilling, Surf. Coat. Technol. 94-95 (1997) 603–609.
[12] W.D. Sproul, R. Rothstein, High rate reactively sputtered TiN coatings on high speed steel drills, Thin Solid Films 126 (1985) 257–263.
[13] J.E. Sundgren, Structure and properties of TiN coatings, Thin Solid Films 128 (1985) 21–44, https://doi.org/10.1016/0040-6090(85)90333-5.
[14] J. Musil, L. Bardo, A. Rajsk, J. Vysko, B. Doleff, G. Lonar, K. Daiourek, V. Kubi, TiN coatings prepared by D.C. reactive magnetron sputtering, Thin Solid Films 136 (1986) 229–239.
[15] H.C. Barshilia, M.S. Prakash, A. Jain, K.S. Rajam, Structure, hardness and thermal stability of TiAlN and nanolayered TiAlN/CrN multilayer films, Vacuum 77 (2005) 169–179, https://doi.org/10.1016/j.vacuum.2004.08.020.
[16] W.-D. Muenz, Titanium aluminum nitride films: a new alternative to TiN coatings, J. Vac. Sci. Technol. A 4 (6) (1986) 2717–2725.
[17] P.H. Mayrhofer, D. Music, J.M. Schneider, Ab initio calculated binodal and spinodal of cubic Ti 1-xAl xN, Appl. Phys. Lett. 88 (2006), https://doi.org/10.1063/1.2177630.
[18] P.H. Mayrhofer, A. Hörling, L. Karlsson, J. Sjölén, T. Larsson, C. Mitterer, L. Hultman, Self-organized nanostructures in the Ti-Al-N system, Appl. Phys. Lett. 83 (2003) 2049–2051, https://doi.org/10.1063/1.1608464.
[19] O. Knotek, T. Leyendeckers, On the structure of (Ti, AI)N-PVD coatings, J. Solid State Chem. 70 (1987) 318–322.
[20] T. Chen, Z. Xie, F. Gong, Z. Luo, Z. Yang, Correlation between microstructure evolution and high temperature properties of TiAlSiN hard coatings with different Si and Al content, Appl. Surf. Sci. 314 (2014) 735–745, https://doi.org/10.1016/j.apsusc.2014.06.057.
[21] L. Rebouta, F. Vaz, M. Andritschky, M.F. Da Silva, Oxidation resistance of (Ti,AI,Zr, Si)N coatings in air, Surf. Coat. Technol. 76-77 (1995) 70–74.

[22] D.A. Colombo, A.D. Mandri, M.D. Echeverría, J.M. Massone, R.C. Dommarco, Mechanical and tribological behavior of Ti / TiN and TiAl / TiAlN coated austempered ductile iron, Thin Solid Films 647 (2018) 19–25, https://doi.org/10.1016/j.tsf.2017.12.014.
[23] S. Paldey, S.C. Deevi, Single layer and multilayer wear resistant coatings of (Ti,Al)N: a review, Materials Science and Engineering: A 342 (2002) 58–79. www.elsevier.com/locate/msea.
[24] M. Stueber, H. Holleck, H. Leiste, K. Seemann, S. Ulrich, C. Ziebert, Concepts for the design of advanced nanoscale PVD multilayer protective thin films, J. Alloys Compd. 483 (2009) 321–333, https://doi.org/10.1016/j.jallcom.2008.08.133.
[25] T. Mori, M. Noborisaka, T. Watanabe, T. Suzuki, Oxidation resistance and hardness of TiAlSiN/CrAlYN multilayer films deposited by the arc ion plating method, Surf. Coat. Technol. 213 (2012) 216–220, https://doi.org/10.1016/j.surfcoat.2012.10.050.
[26] M. Shinn, L. Hultman, S.A. Barnett, Growth, structure, and microhardness of epitaxial TiN/NbN superlattices, J. Mater. Res. 7 (1992) 901–911, https://doi.org/10.1557/JMR.1992.0901.
[27] P.E. Hovsepian, D.B. Lewis, W.D. Münz, Recent progress in large scale manufacturing of multilayer/superlattice hard coatings, Surf. Coat. Technol. 133–134 (2000) 166–175, https://doi.org/10.1016/S0257-8972(00)00959-2.
[28] R. Ramadoss, N. Kumar, S. Dash, D. Arivuoli, A.K. Tyagi, Wear mechanism of CrN/NbN superlattice coating sliding against various counterbodies, Int. J. Refract. Met. Hard Mater. 41 (2013) 547–552, https://doi.org/10.1016/j.ijrmhm.2013.07.005.
[29] R. Hahn, M. Bartosik, M. Arndt, P. Polcik, P.H. Mayrhofer, Annealing effect on the fracture toughness of CrN/TiN superlattices, Int. J. Refract. Met. Hard Mater. 71 (2018) 352–356, https://doi.org/10.1016/j.ijrmhm.2017.11.008.
[30] W.D. Sproul, High-rate reactive DC magnetron sputtering of oxide and nitride superlattice coatings, Vacuum 51 (1998) 641–646, https://doi.org/10.1016/s0042-207x(98)00265-6.
[31] U. Helmersson, S. Todorova, S.A. Barnett, J.E. Sundgren, L.C. Markert, J.E. Greene, Growth of single-crystal TiN/VN strained-layer superlattices with extremely high mechanical hardness, J. Appl. Phys. 62 (1987) 481–484, https://doi.org/10.1063/1.339770.
[32] P.Eh. Hovsepian, D.B. Lewis, Q. Luo, W.-D. Münz, P.H. Mayrhofer, C. Mitterer, Z. Zhou, W.M. Rainforth, TiAlN based nanoscale multilayer coatings designed to adapt their tribological properties at elevated temperatures, Thin Solid Films 485 (2005) 160–168, https://doi.org/10.1016/j.tsf.2005.03.048.
[33] M. Stueber, C. Ziebert, H. Leiste, S. Ulrich, C. Sanz, E. Fuentes, I. Etxarri, M. Solay, A. Garcia, P.B. Barna, R. Hovsepian, Wear studies and cutting tests of Ti-Al-N-C nanocomposite coatings in milling operations technical communication, Mach. Sci. Technol. 13 (2009) 122–141, https://doi.org/10.1080/10910340902782687.
[34] M.S. Ibrahim, M.H. Sulaiman, R. Samin, Y. Yaakob, S.L. Kamis, M.J.M. Ridzuan, A. A. Pauzi, N.A. Sukindar, K. Bienk, Tool wear of DLC coating as top-layered to CrN, TiAlSiN, TiAlN coatings in machining of steel and aluminum alloys, Wear 558–559 (2024), https://doi.org/10.1016/j.wear.2024.205574.
[35] ASTM G-40-99, Wear and Erosion 1, ASTM Standards i (2016) 1–9.
[36] Astm G 98-02, Standard test method for galling resistance of materials, Standards 02 (2002) 1–4, https://doi.org/10.1520/G0098-17.2.
[37] K.-D. Bouzakis, N. Vidakis, N. Michailidis, T. Leyendecker, G. Erkens, G. Fuss, Quantification of properties modification and cutting performance of ($Ti_{1-x}Al_x$)N coatings at elevated temperatures, Surf. Coat. Technol. 120-121 (1999) 34–43. www.elsevier.nl/locate/surfcoat.
[38] A. Jamali, A. Kashyap, J. Schneider, M. Stueber, V. Schulze, Grey-box modelling for tool wear prediction in milling: fusion of finite element insights, time-resolved cutting signals and metaheuristic feature selection, Wear 580–581 (2025) 206292, https://doi.org/10.1016/j.wear.2025.206292.
[39] A. Jamali, A. Kashyap, F. Rümenapf, N.F.L. Dias, W. Tillmann, J. Schneider, M. Stüber, V. Schulze, Grey-box model-integrating tribology descriptor for tool wear prediction in milling, CIRP Ann. (2026), https://doi.org/10.1016/j.cirp.2026.04.087.
[40] A. Anders, A structure zone diagram including plasma-based deposition and ion etching, Thin Solid Films 518 (2010) 4087–4090, https://doi.org/10.1016/j.tsf.2009.10.145.
[41] H.A. Jehn, S. Hofmann, V.-E. Rockborn, W.-D. Muenz, Morphology and properties of sputtered (Ti,AI)N layers on high speed steel substrates as a function of deposition temperature and sputtering atmosphere, J. Vac. Sci. Technol. A (1986) 2701–2705.
[42] Q. Luo, S. Yang, K.E. Cooke, Hybrid HIPIMS and DC magnetron sputtering deposition of TiN coatings: deposition rate, structure and tribological properties, Surf. Coat. Technol. 236 (2013) 13–21, https://doi.org/10.1016/j.surfcoat.2013.07.003.
[43] A. Kashyap, A.P. Harsha, P. Kondaiah, H.C. Barshilia, Study on galling behaviour of HiPIMS deposited Mo/DLC multilayer coatings at ambient and elevated temperature, Wear 498–499 (2022) 204327, https://doi.org/10.1016/j.wear.2022.204327.
[44] I. Petrov, L. Hultman, U. Helmersson, J.-E. Sundgren, J.E. Greene, Microstructure Modification of TiN by Ion Bombardment during Reactive Sputter Deposition, 1989.
[45] L. Hultman, G. Håkansson, U. Wahlstram, J.-E. Sundgren, I. Petrov, F. Adibi, J. E. Greene, Transmission electron microscopy studies of microstructural evolution, defect structure, and phase transitions in polycrystalline and epitaxial TiN, AlN, and TiN films grown by reactive magnetron sputter deposition, Thin Solid Films 205 (1991) 151–164.
[46] G. Hakansson, J. Sundgren, D. Mcintyre, J.E. Greene, W. MiiNZ Leybold-Heraeus GmbH, Microstructure and physical properties of polycrystalline metastable Ti, Thin Solid Films 153 (1987) 55–65.
[47] J.M. Lackner, W. Waldhauser, R. Ebner, J. Keckés, T. Schöberl, Room temperature deposition of (Ti,Al)N and (Ti,Al)(C,N) coatings by pulsed laser deposition for tribological applications, Surf. Coat. Technol. 177–178 (2004) 447–452, https://doi.org/10.1016/S0257-8972(03)00911-3.
[48] A.E. Diniz, Á.R. Machado, J.G. Corrêa, Tool wear mechanisms in the machining of steels and stainless steels, Int. J. Adv. Manuf. Technol. 87 (2016) 3157–3168, https://doi.org/10.1007/s00170-016-8704-3.
[49] G. Dixon, R.N. Wright, M. Lee, Processes involved in the wear of cemented carbide tools, Wear 104 (1985) 157–171, https://doi.org/10.1016/0043-1648(85)90060-2.
[50] S. Saketi, U. Bexell, J. Östby, M. Olsson, On the diffusion wear of cemented carbides in the turning of AISI 316L stainless steel, Wear 430–431 (2019) 202–213, https://doi.org/10.1016/j.wear.2019.05.010.
[51] G.J. Liu, Z.C. Zhou, X. Qian, W.H. Pang, G.H. Li, G.Y. Tan, Wear mechanism of cemented carbide tool in high speed milling of stainless steel, Chinese Journal of Mechanical Engineering (English Edition) 31 (2018), https://doi.org/10.1186/s10033-018-0298-2.
[52] V.F.C. Sousa, F.J.G. Da Silva, G.F. Pinto, A. Baptista, R. Alexandre, Characteristics and wear mechanisms of TiAlN-based coatings for machining applications: a comprehensive review, Metals (Basel) 11 (2021) 1–49, https://doi.org/10.3390/met11020260.
[53] R. Ramadoss, N. Kumar, R. Pandian, S. Dash, T.R. Ravindran, D. Arivuoli, A. K. Tyagi, Tribological properties and deformation mechanism of TiAlN coating sliding with various counterbodies, Tribol. Int. 66 (2013) 143–149, https://doi.org/10.1016/j.triboint.2013.05.001.
[54] M.H. Staia, M. D'Alessandria, D.T. Quinto, F. Roudet, M. Marsal Astort, High-temperature tribological characterization of commercial TiAlN coatings, J. Phys. Condens. Matter 18 (2006), https://doi.org/10.1088/0953-8984/18/32/S04.